Supplementary Information: Loopy Lévy flights enhance tracer diffusion in active suspensions

Kiyoshi Kanazawa
Faculty of Engineering, Information and Systems, University of Tsukuba, Tennodai, Tsukuba, Ibaraki 305-8577, Japan

Tomohiko G. Sano
Flexible Structures Laboratory, Institute of Mechanical Engineering, École polytechnique fédérale de Lausanne, Lausanne, CH-1015, Switzerland.

Andrea Cairoli
Department of Bioengineering, Imperial College London, London SW7 2AZ, UK

Adrian Baule
School of Mathematical Sciences, Queen Mary University of London, London E1 4NS, UK

This Supplementary Information is organized as follows. In Section I, we describe the details of the protocol used for the numerical simulations of the microscopic model (1). In Section II, we present ideas and mathematical tools to derive the coarse-grained description of the tracer dynamics in terms of the coloured Poisson model (3) within the framework of the kinetic theory of dilute gases. Specifically, we derive the collision rule and the intensity of the underlying Poisson process in Section II A, we discuss how to solve perturbatively the two-body swimmer-tracer scattering problem in Section II B, and we derive asymptotic formulas for the force shape function (FSF) in Sections II C, II D. In Section III, we characterize the coloured Poisson noise (3) by means of its characteristic functional. This is a fundamental mathematical tool that allows us to study the tracer displacement statistics, in terms of its probability distribution function (PDF), mean square displacement (MSD), and non-Gaussian parameter (NGP). Asymptotic formulas in both the Holtsmark and scattering regimes are also presented for all these quantities (Sections III A and III B respectively). In Section III C we discuss the generalisation of the theory to D-dimensions and more general non-dipolar hydrodynamic flows; in particular, we derive general formulas for the scaling exponents of the tracer displacement PDF. In Section IV we review the definition of Lévy processes and relate it to the context outlined in the manuscript. In Section V, we discuss some ambiguities arising during the assessment of the scaling behaviour of the tracer displacement statistics from experimental data, and highlight how statistical sampling may need to be improved to resolve them. Finally, Section VI contains all the technical calculations. In details, we derive the FSF for the specific case of the stresslet hydrodynamic force in Section VI A. In Section VI B, we derive the characteristic functional of the coloured Poisson noise. In Section VI C, we discuss the consistency between our own description of the tracer statistics and that provided by the static Holtsmark theory at short timescales. Sections VI D, VI E, and VI F contain the derivation of the asymptotic formulas for the tracer displacement PDF respectively in the Holtsmark, scattering and central limit theorem (CLT) regimes, while those for the MSD and the NGP are reported in Sections VI G and VI H. Details on the derivation of the asymptotic tail behaviour of Lévy-type distributions are provided in Section VI I. The summary of this Supplementary Information is given by Table S1.

I. PROTOCOL FOR NUMERICAL SIMULATIONS

To confine the tracer and the active swimmers in the square box, we add wall-potentials $U_{\rm wall} = e_{\rm wall} r_{\rm wall}^{-12}/12$ near the boundaries $0 < r_{\rm wall} < 2b^*$ to Eqs. (1), where we define the distance from the boundary $r_{\rm wall}$ and we set $e_{\rm wall}/(\Gamma v_{\rm A} b^*) = 1.0 \times 10^3$. In the large system size limit $L \to \infty$, the detail of the wall (i.e., the value of $e_{\rm wall}$) is irrelevant to the main results. Thus our model has the following four independent parameters: $(p/\Gamma, v_{\rm A}, d, \rho)$, where we note that p always appears in the form of p/Γ. Considering the definitions $b^* \equiv \sqrt{|p|/(\Gamma v_{\rm A})}$ and $\tau_{\rm H} \equiv b^*/v_{\rm A}$, we can take a set of independent parameters $(b^*, \tau_{\rm H}, d, \rho)$ and the sign of p (i.e., pusher or puller). In the following, we choose the units of length and time by setting $b^* = 1$ and $\tau_{\rm H} = 1$. The equations of motion are integrated by the Adams-Bashforth method [36] after rescaling them appropriately with the time step $1.0 \times 10^{-2}\tau_{\rm H}$. We note that the action-reaction principle is not incorporated in the model (1), as we are interested in the degrees of freedom of passive and active particles only (for the whole system, i.e., including also those of the fluid, it should be accounted for).

a. For pusher swimmers. Here we summarize parameters adopted in the numerical simulation for Fig. 1b, 2, and 3 in the main text for pusher swimmers ($p < 0$). We set $b^*/d = 1.0$ and $m = 80$ with the number of swimmers m. The box size is set to be $L/d = 1600$ in Fig. 3a, whereas it is varied among $L/d = 1000$, 1200, and 1600 in Fig. 3b

Section in SI	Contents	Related figures/equations in main text
Sec. I	Details of the numerical simulations	Figs. 1–3
Sec. II	Kinetic framework for the coloured Poisson model	Eq. (3) and Figs. 2–3
Sec. II A	Collision rule and intensity	Eq. (3) and Figs. 1c and 2a
Sec. II B	Two-body scattering problem	Figs. 1c and 2
Sec. II C	Asymptotic method for the force shape function	Eq. (3) and Figs. 1c and 2
Sec. II D	Force shape function for the stresslet force	Eq. (3) and Figs. 1c and 2
Sec. III	Framework of characteristic functional analysis	Eq. (4) and Fig. 3
Sec. III A	Mean square displacement formula	Fig. 3b
Sec. III B	Non-Gaussian parameter formula	Fig. 3c
Sec. III C	Derivation of the scaling exponents for general D-dimensional active flows	Eq. (4)
Sec. IV	A brief review on Lévy processes	Eqs. (3) and (4)
Sec. V	Discussion on experimental validation of power-law scaling	Eq. (4) and Fig. 3a
Sec. VI	Technical Calculations	Eqs. (3) and (4)
Sec. VI A	Derivation of the force shape function for the stresslet force	Eqs. (3) and Figs. 2b and 2c
Sec. VI B	Characteristic functional for the coloured Poisson model	Eq. (4) and Fig. 3
Sec. VI C	Predictions by the Holtsmark theory	Eq. (4) and Fig. 3a
Sec. VI D	Short-time behaviour for displacement statistics	Eq. (4) and Fig. 3a
Sec. VI E	Intermediate-time behaviour for displacement statistics	Eq. (4) and Fig. 3a
Sec. VI F	Long-time behaviour for displacement statistics	Eq. (4) and Fig. 3a
Sec. VI G	Detailed calculation for the mean square displacement	Fig. 3b
Sec. VI H	Detailed calculation for the non-Gaussian parameter	Fig. 3c
Sec. VI I	Derivation of the asymptotic tail behaviour of Lévy-type distributions	Eq. (4) and Sec. VI D and VI E

TABLE S1: Summary of the Supplementary Information

and 3c. The simulation time was $1.01\tau_{\rm C}$ for the PDF ($0.10-0.41\tau_{\rm C}$ for the MSD and NGP) in the main text. We run the simulation from different initial conditions 960 times for the PDF (64 times for MSD and NGP) and the errorbar represents the standard error among the ensembles.

b. For puller swimmers. We performed a numerical simulation for puller swimmers ($p>0$) as shown in Fig. S1. We set $b^*/d=0.25$ and $m=80$. The box size is set to be $L/d=800$ in Fig. S1a, whereas it is varied among $L/d=800$, 1000, and 1200 in Fig. S1b and S1c. The simulation time step was $8.04\tau_{\rm C}$ for the PDF ($0.23-0.80\tau_{\rm C}$ for the MSD and NGP). We run the simulation from different initial conditions 640 times for the PDF (64 times for MSD and NGP) and the errorbar represents the standard error among the ensembles.

We note that an instability of the simulation was observed if p/Γ is set to be much larger than realistic values used in experiments, since the puller interaction is attractive around the core (i.e., the tracer particle can be trapped by the attractive force for sufficiently large p and consequently be dragged through a long distance by a swimmer). This numerical artefact is avoided by imposing the condition $p/d^2<v_{\rm A}\Gamma$, which is equivalent to $d>b^*$, whereby the propelling force of the swimmer is always stronger than the attractive force and thus the tracer cannot catch up with the swimmer finally. We note that this condition is consistent with the estimated values in real experiments as discussed in the main text.

c. Numerical scheme for integration. We numerically integrate the equations of motion up to the time $1.01\tau_{\rm C}$ by using the super computer (Cray XC40) system at the Yukawa Institute for Theoretical Physics (Kyoto University, Japan) and calculate the statistics of tracer displacement with different time windows Δt and $64-960$ different initial conditions.

To validate that the results are insensitive to the choice of m, we perform the simulation for pusher swimmers varying m, fixing the density $\rho b^{*3}/L^3=1.95\times10^{-8}$. In Fig. S2, we plot the numerical results of CDF for (a) $m=40$, (b) $m=80$, (c) $m=160$. We average the data between (a, b) 640 and (c) 320 different initial conditions and the errorbar represents the standard error among the ensembles.

We verified that the tracer statistics is insensitive to the choice of boundary conditions by increasing L and m, while keeping fixed the number density of active swimmers $\rho=m/L^3$. In contrast, increasing the density or the area fraction (2D) significantly affects the dynamics of the tracer. In particular, we expect to observe cage effects which slow down the motion of the tracer. However, detailed investigation of these effects goes beyond the scope of the present letter, and will be addressed in future publications.

We refer to the Supplementary Movie as visualization of the dynamics of our numerical simulation for pusher swimmers. To generate the Supplementary Movie, the equations of motion are integrated up to the time $1.57\times10^{-4}\tau_{\rm C}$. The size of the simulation box is set to be $L/d=6400$. The rest of parameters are fixed to be the same as above.

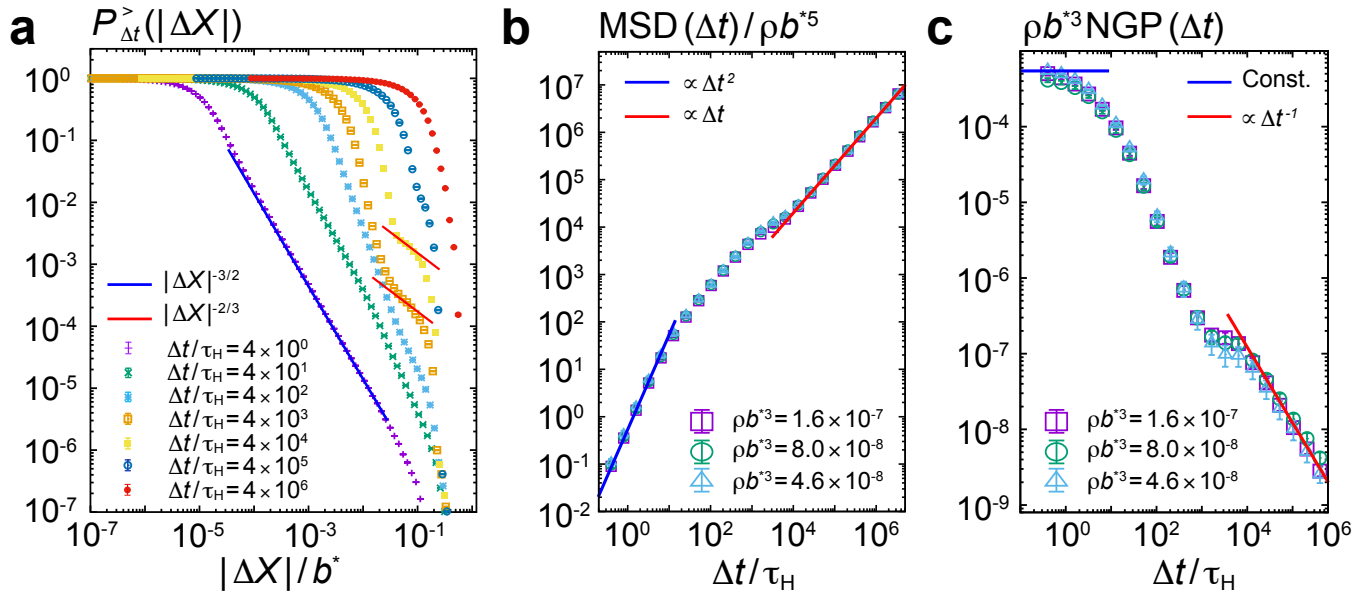

FIG. S1: Numerical simulation for puller swimmers. (a) The complementary cumulative probability distribution (CDF) for the displacement $|\Delta X|$, defined by $P^{>}_{\Delta t}(|\Delta X|) \equiv \int_{|\Delta X|}^{\infty} \mathrm{d}(\Delta X') P(|\Delta X'|)$. $P^{>}_{\Delta t}(|\Delta X|)$ shows the power-law behaviour $P^{>}_{\Delta t}(|\Delta X|) \propto |\Delta X|^{-\alpha_H+1}$ for short time $\Delta t \ll \tau_H$ and $P^{>}_{\Delta t}(|\Delta X|) \propto |\Delta X|^{-\alpha_S+1}$ for intermediate time $\tau_H \ll \Delta t \ll \tau_C$ with $\alpha_H = 5/2$ and $\alpha_S \equiv 5/3$ for large ΔX. For a long time $\tau_C \ll \Delta t$, the CDF converges to the Gaussian due to the central limit theorem. (b) The MSD exhibits the crossover from ballistic to diffusive behaviour and the data collapse upon rescaling by $1/(\rho b^{*5})$. (c) The NGP decreases according to Δt^{-1}, showing the data collapse upon rescaling by ρb^{*3}. Therefore, the theory does not predict any qualitative difference in the tracer displacement statistics between suspensions of puller and pusher swimmers in dilute condition. Error bars denote ± 1 s.e.m..

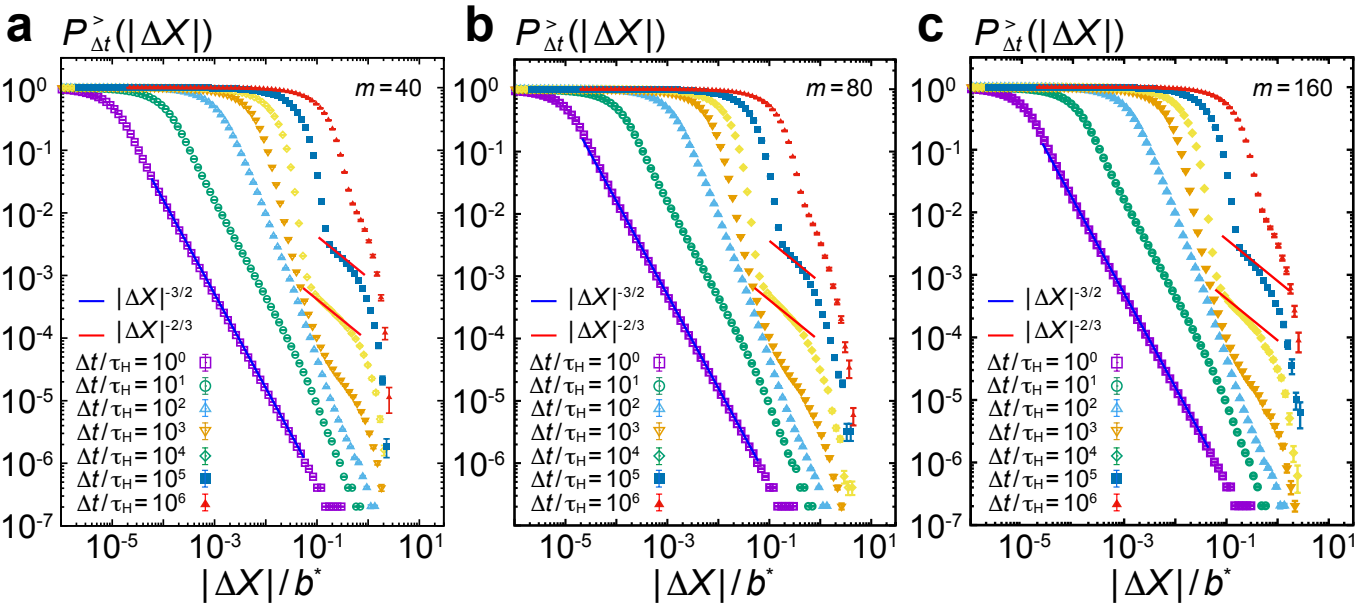

FIG. S2: Numerical simulation for pusher swimmers with different m but fixed ρ. We have plotted the CDF for the displacement $|\Delta X|$ for (a) $m = 40$, (b) $m = 80$, and (c) $m = 160$. Error bars denote ± 1 s.e.m..

II. KINETIC DERIVATION OF THE COLOURED LÉVY PROCESS

The microscopic dynamics specified by Eqs. (1) includes the self-propelling force for the swimmers, that clearly drives the system out of equilibrium. Therefore, the conventional framework of equilibrium statistical mechanics

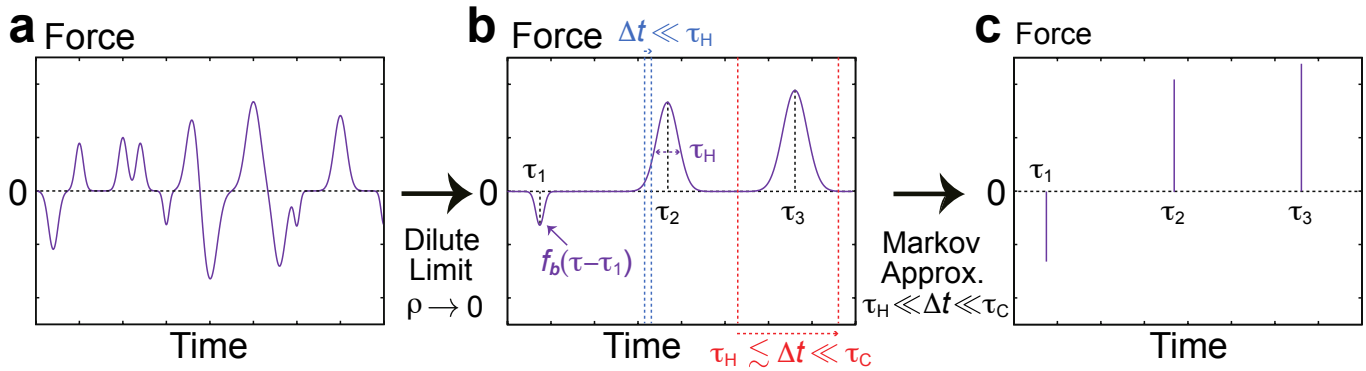

FIG. S3: (a) Schematic of the force time series exerted on the tracer by the active swimmers for high-density conditions. Here, many-body interactions between tracer and swimmers cannot be neglected. (b) In the low-density case, instead, two-body interactions become dominant and the tracer dynamics is effectively described by a succession of two-body scattering events at random time points $\{\tau_i\}$. The force exerted on the tracer during each scattering, i.e., the force shape function $f_{\boldsymbol{b}}(t)$, is specified by solving the two-body scattering problem perturbatively. Its functional form depends on the scattering characteristic parameters $\boldsymbol{b} \equiv (b, \theta, \phi, \phi')$. For simplicity, here it is assumed Gaussian. The effect of different observation timescales is pictorially shown. For $\Delta t \ll \tau_{\rm H}$ (Holtsmark regime), the tracer only feels static forces (because the motion of active particles can be effectively neglected), whose strength depends on the initial distribution of the swimmers. Only for longer timescales $\tau_{\rm H} \lesssim \Delta t \ll \tau_{\rm C}$ the tracer can appreciate the full time evolution of the scattering events. (c) For $\tau_{\rm H} \ll \Delta t \ll \tau_{\rm C}$ (scattering regime), the force shape function can be approximated as the Dirac δ-function with varying amplitudes. Therefore, at this timescale our model reduces to a Markovian compound Poisson process with power-law distributed jump lengths, effectively equivalent to a Lévy flight (See Section IV).

(e.g., the Gibbs ensemble formulation) cannot be applied to understand the resulting nonequilibrium dynamics of the tracer. Nevertheless, the framework of the kinetic theory of dilute gases [37] remains available even for such an out-of-equilibrium state when the active bath, which plays the role of the gas here, is sufficiently dilute.

To understand this idea, we consider a gedanken-experiment where we change the density of swimmers from the dense to the dilute regime and study the resulting stochastic dynamics of the tracer (Fig. S3). When the swimmers are dense, the tracer motion is driven by its generally multi-body interactions with the swimmers, such that it typically exhibits a complex dynamical behaviour (see schematics in panel a). Conversely, when the swimmers are sufficiently dilute, the two-body interactions become dominant to leading-order approximation, and thus the tracer exhibits a much simpler dynamics (see schematics in panel b), where scattering times (i.e., the time when a swimmer passes by the tracer with its velocity orthogonal to the swimmer-tracer distance vector) can be identified individually.

Within the framework of kinetic theory, these events that are associated with two-body swimmer-tracer interactions can be mathematically captured as a Poisson injection process characterised by a sequence of collision times $\{\tau_i\}$ for $i = 1, \ldots, N(t)$, where the Poisson process N specifies the number of scatterings up to time t, and by the force-shape function (FSF) $f_{\boldsymbol{b}_i}(t)$ with $\boldsymbol{b}_i \equiv (b_i, \theta_i, \phi_i, \phi_i')$, which describes the force exerted on the tracer during the two-body scattering event and whose functional form is specified by the scattering impact parameter b_i and injection angles $(\theta_i, \phi_i, \phi_i')$. Here the scattering point is identified by the spherical coordinate system (b, θ, ϕ) and the injection angle of the swimmer is identified by ϕ' on the plane spanned by $\boldsymbol{e}_\theta$ and $\boldsymbol{e}_\phi$ (see Fig. S4b). We note that the Poisson injection is characterized by the intensity $\lambda(\boldsymbol{b})$ conditional on $\boldsymbol{b} \equiv (b, \theta, \phi, \phi')$. Both λ and the FSF $f_{\boldsymbol{b}}(t)$ need to be specified from the microscopic dynamics (1) (see below). We anticipate here that $\lambda(\boldsymbol{b})d\boldsymbol{b} \propto b$, such that $\lim_{L\to\infty} \int \mathrm{d}\boldsymbol{b}\lambda(\boldsymbol{b}) = \infty$. Therefore, this noise is a non Markovian Poisson process with infinite intensity, a generalisation of the widely known Campbell process [29].

The pictorial description of the tracer coarse-grained dynamics shown in panel (b) also elucidates the role played by the observation timescale on the measured statistics of the tracer displacements. In fact, for timescales short enough that the motion of the swimmers can be effectively neglected, i.e., for $\Delta t \ll \tau_{\rm H}$ (Holtsmark regime), the tracer only feels static forces from its surrounding medium, whose strength depends on its distance from each of the active particles that generate such forces. As the active particles are initially randomly distributed, this is equivalent to considering an isotropic distribution of static forces [10, 23, 24], as previously discussed by Holtsmark in the context of gravitation [25]. On the contrary, for timescales long enough that the tracer can appreciate the full time evolution of the scattering events, i.e., for $\tau_{\rm H} \ll \Delta t \ll \tau_{\rm C}$ (scattering regime), the statistical features of its dynamics are only captured by the kinetic picture outlined above. At this timescale the theory predicts that the coloured Poisson process is equivalent to a compound Poisson process with power-law distributed jump lengths (see panel c), which thus suggests that the well known Lévy flight model [38] is valid as an effective description of the tracer dynamics.

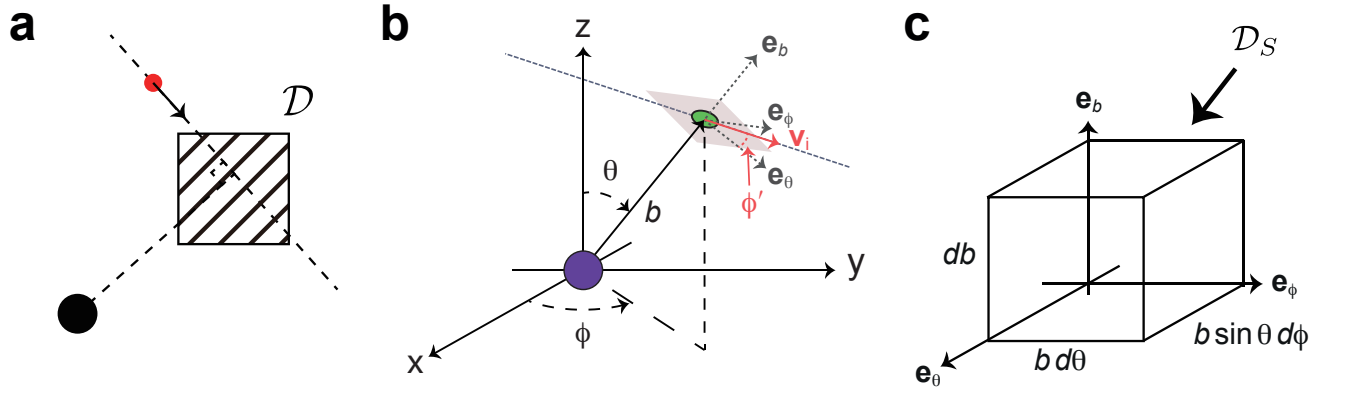

FIG. S4: (a) Scattering event within the domain $\mathcal{D}$. A scattering occurs when the velocity of the active particle is orthogonal to the radial vector from the passive tracer, i.e., $[\boldsymbol{x}_i - \boldsymbol{X}] \cdot \boldsymbol{v}_i = 0$ and $\boldsymbol{x}_i \in \mathcal{D}$. (b) Spherical coordinate system used in this SI. Auxiliary orthogonal unit vectors $\boldsymbol{e}_b$, $\boldsymbol{e}_\theta$ and $\boldsymbol{e}_\phi$ are also defined. Considering the scattering condition, the swimmer moves on the plane spanned by $\boldsymbol{e}_\theta$ and $\boldsymbol{e}_\phi$. The scattering point (i.e., the nearest point during the passing-by process) and the injection angle in this plane are designated by (b, θ, ϕ) and ϕ' respectively. (c) Intensity of scattering events within the infinitesimal domain $\mathcal{D}_S$, whose volume element is given by $\mathrm{d}\boldsymbol{x}_i = b^2 \sin\theta \, \mathrm{d}b \, \mathrm{d}\theta \, \mathrm{d}\phi$.

We remark that a natural truncation of this jump length distribution appears for finite d at every timescale Δt: large displacements are caused by large hydrodynamic forces, whose amplitudes are widely distributed because of the power-law nature of the interaction force (2). However, its maximum amplitude has the order of p/d^2 for finite d, which is natural since a swimmer cannot generate an infinitely strong hydrodynamic force. This truncation in the force amplitude induces a corresponding truncation in the displacement PDF and thus implies that the variance of the tracer displacements is always finite.

Finally, at long timescales $\Delta t \gg \tau_\mathrm{C}$, interaction events between the tracer and the swimmers at distances smaller than the characteristic lengthscale d become more and more relevant (in a probabilistic sense). For these events the interaction force is characterised by hydrodynamic non-dipolar near-field contributions and hard-core interactions, which induce a different displacement on the tracer than what is predicted by our coloured Poisson process. At the same time, for such long timescales, the tracer displacement is due to an accumulation of a large number of interaction events between the tracer and the swimmers that can be captured quantitatively in terms of the central limit theorem. We thus expect the tracer displacement statistics to converge to a Gaussian at such timescales (see Section VI F).

A. Scattering rule and intensity of the Poisson injection process

Here we derive the intensity of scattering events by active swimmers based on kinetic theory. Let us consider scattering events within a domain $\mathcal{D}$; these are specified for an active particle by the condition

$$[\boldsymbol{x}_i(\tau_{i;j}) - \boldsymbol{X}(\tau_{i;j})] \cdot \boldsymbol{v}_i(\tau_{i;j}) = 0, \quad \boldsymbol{x}_i(\tau_{i;j}) \in \mathcal{D} \tag{S1}$$

with the j-th scattering time $\tau_{i;j}$ exerted by the i-th active swimmer (see Fig. S4a). The intensity of the Poisson noise is thus given by the following formula

$$\lambda_\mathcal{D} = \left\langle \sum_{i=1}^{m} \sum_{j=1}^{\infty} \delta(t - \tau_{i;j}) \right\rangle \tag{S2}$$

with $\langle \cdot \rangle$ the average over the position-velocity distribution of active particles. Here we use an identity of the δ-function:

$$\delta(g(t)) = \sum_j \frac{\delta(t - \tau_j)}{|g'(\tau_j)|}, \tag{S3}$$

where τ_j satisfies the equation $g(\tau_j) = 0$ and $\tau_j < \tau_{j+1}$. Setting $g \equiv (\boldsymbol{x}_i - \boldsymbol{X}) \cdot \boldsymbol{v}_i$, we find that $g'(\tau_{i;j}) = |\boldsymbol{v}_i|^2$, such that the identity yields the following relation

$$\sum_{j=1}^{\infty} \delta(t - \tau_{i;j}) = |\boldsymbol{v}_i|^2 \delta((\boldsymbol{x}_i - \boldsymbol{X}) \cdot \boldsymbol{v}_i), \tag{S4}$$

which leads to

$$\lambda_{\mathcal{D}} = m|\boldsymbol{v}_i|^2 \left\langle \delta([\boldsymbol{x}_i - \boldsymbol{X}] \cdot \boldsymbol{v}_i) \right\rangle = m|\boldsymbol{v}_i|^2 \int_{\mathcal{D}} \mathrm{d}\boldsymbol{x}_i \int_{\mathbb{R}^3} \mathrm{d}\boldsymbol{v}_i \delta((\boldsymbol{x}_i - \boldsymbol{X}) \cdot \boldsymbol{v}_i) P(\boldsymbol{x}_i, \boldsymbol{v}_i). \tag{S5}$$

As position and velocity of active particles are independent random variables, their joint distribution can be factorised. We further assume that the marginal position distribution for the ith active particle is spatially uniform and similarly that the marginal velocity distribution is spherically uniform, i.e.,

$$P(\boldsymbol{x}_i, \boldsymbol{v}_i) = \frac{1}{4\pi v_A^2 L^3} \delta(|\boldsymbol{v}_i| - v_A). \tag{S6}$$

By taking the thermodynamic limit $L \to \infty$ with the density kept constant $\rho = m/L^3$, we obtain

$$\lambda_{\mathcal{D}} = \frac{\rho}{4\pi} \int_{\mathcal{D}} \mathrm{d}\boldsymbol{x}_i \int_{\mathbb{R}^3} \mathrm{d}\boldsymbol{v}_i \delta((\boldsymbol{x}_i - \boldsymbol{X}) \cdot \boldsymbol{v}_i) \delta(|\boldsymbol{v}_i| - v_A). \tag{S7}$$

We next introduce the spherical coordinate system (b, θ, ϕ) to designate the scattering point $\boldsymbol{x}_i$ (Fig. S4b):

$$\boldsymbol{x}_i - \boldsymbol{X} = \begin{pmatrix} b\sin\theta\cos\phi \\ b\sin\theta\sin\phi \\ b\cos\theta \end{pmatrix} \tag{S8}$$

with $b \in [0, \infty)$, $\theta \in [0, \pi]$, and $\phi \in (-\pi, \pi]$. We also define orthogonal unit vectors related to the spherical coordinates,

$$\boldsymbol{e}_b \equiv \frac{\partial(\boldsymbol{x}_i - \boldsymbol{X})}{\partial b} = \begin{pmatrix} \sin\theta\cos\phi \\ \sin\theta\sin\phi \\ \cos\theta \end{pmatrix}, \ \boldsymbol{e}_\theta \equiv \frac{1}{b}\frac{\partial(\boldsymbol{x}_i - \boldsymbol{X})}{\partial \theta} = \begin{pmatrix} \cos\theta\cos\phi \\ \cos\theta\sin\phi \\ -\sin\theta \end{pmatrix}, \ \boldsymbol{e}_\phi \equiv \frac{1}{b\sin\theta}\frac{\partial(\boldsymbol{x}_i - \boldsymbol{X})}{\partial \phi} = \begin{pmatrix} -\sin\phi \\ \cos\phi \\ 0 \end{pmatrix}, \tag{S9}$$

which satisfy the orthogonal condition $\boldsymbol{e}_b \cdot \boldsymbol{e}_\theta = \boldsymbol{e}_b \cdot \boldsymbol{e}_\phi = \boldsymbol{e}_\theta \cdot \boldsymbol{e}_\phi = 0$. Based on the formula (S7), we calculate the intensity of scattering events within the infinitesimal domain $\mathcal{D}_S \equiv \{[\boldsymbol{x}_i - \boldsymbol{X}](\tilde{b}, \tilde{\theta}, \tilde{\phi}) | \tilde{b} \in [b, b + \mathrm{d}b), \tilde{\theta} \in [\theta, \theta + \mathrm{d}\theta), \tilde{\phi} \in [\phi, \phi + \mathrm{d}\phi]\}$ (Fig. S4c). By introducing another spherical coordinate system (v_i, θ', ϕ') with $v_i \in [0, \infty)$, $\theta' \in [0, \pi]$, and $\phi' \in (-\pi, \pi]$ for $\boldsymbol{v}_i$ such that

$$\boldsymbol{v}_i = v_i \sin\theta' \cos\phi' \boldsymbol{e}_\theta + v_i \sin\theta' \sin\phi' \boldsymbol{e}_\phi + v_i \cos\theta' \boldsymbol{e}_b, \tag{S10}$$

we obtain

$$\lambda_{\mathcal{D}_S} = \frac{\rho}{4\pi} b^2 \sin\theta \ \mathrm{d}b\,\mathrm{d}\theta\,\mathrm{d}\phi \int_0^\infty v_i^2 \,\mathrm{d}v_i \int_0^\pi \mathrm{d}\theta' \int_0^{2\pi} \mathrm{d}\phi' \delta(b v_i \cos\theta') \delta(v_i - v_A) = \frac{\rho v_A}{2} b \sin\theta \ \mathrm{d}b\,\mathrm{d}\theta\,\mathrm{d}\phi, \tag{S11}$$

where we used the relations $\mathrm{d}\boldsymbol{x}_i = b^2 \sin\theta \ \mathrm{d}b\,\mathrm{d}\theta\,\mathrm{d}\phi$ and $\delta(b v_i \cos\theta') = (b v_i)^{-1} \delta(\theta' - \pi/2)$ (valid for $\theta' \in [0, \pi]$).

So far we studied the intensity of scattering events within the domain $\mathcal{D}_S$. Here we generalize the formulation: let us study the scattering intensity within $\mathcal{D}_S$ conditional on the injection velocity $\boldsymbol{v}_i = \boldsymbol{v}$, which is given by

$$\lambda_{\mathcal{D}_S}(\boldsymbol{v}) = \left\langle \sum_{i=1}^{m} \sum_{j=1}^{\infty} \delta(t - \tau_{i;j}) \delta(\boldsymbol{v} - \boldsymbol{v}_i) \right\rangle = \frac{\rho}{4\pi} b^2 \sin\theta \ \mathrm{d}b\,\mathrm{d}\theta\,\mathrm{d}\phi \, \delta((\boldsymbol{x}_i - \boldsymbol{X}) \cdot \boldsymbol{v}) \delta(|\boldsymbol{v}| - v_A). \tag{S12}$$

By introducing spherical coordinates for $\boldsymbol{v}$ as in Eq. (S10), we obtain

$$\lambda_{\mathcal{D}_S}(\boldsymbol{v}) = \frac{\rho b}{4\pi v_A} \delta(v - v_A) \delta(\theta' - \pi/2) \sin\theta \ \mathrm{d}b\,\mathrm{d}\theta\,\mathrm{d}\phi. \tag{S13}$$

Imposing the conservation of probability $\lambda_{\mathcal{D}_S}(\boldsymbol{v}) d\boldsymbol{v} = \lambda(b, \theta, \phi, v, \theta', \phi') |J_{b,\theta,\phi,v,\theta',\phi'}| \,\mathrm{d}b\,\mathrm{d}\theta\,\mathrm{d}\phi\,\mathrm{d}v\,\mathrm{d}\theta'\,\mathrm{d}\phi'$ with the Jacobian factor for the transformation to spherical coordinates for both $\boldsymbol{x}_i$ and $\boldsymbol{v}$ given by $|J_{b,\theta,\phi,v,\theta',\phi'}| = b^2 v^2 \sin\theta \sin\theta'$ and the volume element $\mathrm{d}\boldsymbol{v} = v^2 \sin\theta' \,\mathrm{d}v\,\mathrm{d}\theta'\,\mathrm{d}\phi'$, we obtain

$$\lambda(b, \theta, \phi, v, \theta', \phi') |J_{b,\theta,\phi,v,\theta',\phi'}| = \frac{\rho v_A}{4\pi} b \sin\theta \delta(v - v_A) \delta(\theta' - \pi/2), \tag{S14}$$

which overall leads to the reduced form of the intensity $\lambda(\boldsymbol{b}) \equiv \lambda(b, \theta, \phi, \phi')$ with $\boldsymbol{b} \equiv (b, \theta, \phi, \phi')$ as

$$\lambda(\boldsymbol{b}) |J_{\boldsymbol{b}}| \equiv \int_0^\infty \mathrm{d}v \int_0^\pi \mathrm{d}\theta' \lambda(b, \theta, \phi, v, \theta', \phi') |J_{b,\theta,\phi,v,\theta',\phi'}| = \frac{\rho v_A}{4\pi} b \sin\theta \tag{S15}$$

with the Jacobian factor $|J_{\boldsymbol{b}}| = b^2 \sin\theta$. Note that the intensity $\lambda(\boldsymbol{b})$ here is nonnegative and that (S15) is consistent with (S11) as $\lambda_{\mathcal{D}_S} = \mathrm{d}b\,\mathrm{d}\theta\,\mathrm{d}\phi \int \mathrm{d}\phi' \lambda(\boldsymbol{b}) |J_{\boldsymbol{b}}|$.

B. Two-body scattering problem

Let us consider the two-body scattering graphically represented in Fig. 1c. According to Eqs. (1), we formulate the two-body scattering problem as the following set of differential equations:

$$\frac{\mathrm{d}\boldsymbol{x}_1}{\mathrm{d}t} = v_\mathrm{A}\boldsymbol{n}_1, \tag{S16a}$$

$$\Gamma\frac{\mathrm{d}\boldsymbol{X}}{\mathrm{d}t} = \boldsymbol{F}(\boldsymbol{x}_1 - \boldsymbol{X}, \boldsymbol{n}_1), \tag{S16b}$$

where the time when the swimmer-tracer distance is orthogonal to the swimmer's velocity is arbitrarily set to zero (i.e., $\boldsymbol{x}_1(0) - \boldsymbol{X}(0) = b\boldsymbol{e}_b$). The vector $\boldsymbol{n}_1 \equiv \cos\phi'\boldsymbol{e}_\theta + \sin\phi'\boldsymbol{e}_\phi$ is the direction of the active swimmer, which satisfies the scattering condition $\boldsymbol{n}_1 \cdot [\boldsymbol{x}_1(0) - \boldsymbol{X}(0)] = 0$. Equation (S16a) is then solved as

$$\boldsymbol{x}_1(t) = b\boldsymbol{e}_b + v_\mathrm{A}t\boldsymbol{n}_1. \tag{S17}$$

Equations (S16) are then reduced to the one-body problem

$$\Gamma\frac{\mathrm{d}\boldsymbol{X}}{\mathrm{d}t} = \boldsymbol{F}(b\boldsymbol{e}_b + v_\mathrm{A}t\boldsymbol{n}_1 - \boldsymbol{X}, \boldsymbol{n}_1). \tag{S18}$$

The parameter set to characterize the scattering is finally given by

$$\boldsymbol{b} \equiv (b, \theta, \phi, \phi'). \tag{S19}$$

The corresponding exact FSF is given by $\boldsymbol{f}_{\boldsymbol{b}}(t) \equiv \boldsymbol{F}(b\boldsymbol{e}_b + v_\mathrm{A}t\boldsymbol{n}_1 - \boldsymbol{X}, \boldsymbol{n}_1)$, where $\boldsymbol{X}$ is the solution of Eq. (S18). According to the definition of $\boldsymbol{F}$ in Eq. (2), the FSF can be divided for the **outer** or **inner layers** as

$$\boldsymbol{f}_{\boldsymbol{b}}(t) \equiv \begin{cases} \boldsymbol{f}_{\boldsymbol{b}}^\mathrm{O}(t) & |\boldsymbol{x}_1 - \boldsymbol{X}| > d \\ \boldsymbol{f}_{\boldsymbol{b}}^\mathrm{I}(t) & |\boldsymbol{x}_1 - \boldsymbol{X}| \le d \end{cases}. \tag{S20}$$

The outer layer FSF $\boldsymbol{f}_{\boldsymbol{b}}^\mathrm{O}$ can be derived as a suitable asymptotic approximation in terms of b^*/b:

$$\boldsymbol{f}_{\boldsymbol{b}}^\mathrm{O}(t) = \boldsymbol{f}_{\boldsymbol{b}}^{\mathrm{O}(1)}(t) + \boldsymbol{f}_{\boldsymbol{b}}^{\mathrm{O}(2)}(t) + \dots, \tag{S21}$$

that is valid for large impact parameter, in the sense that $|\boldsymbol{f}_{\boldsymbol{b}}^{\mathrm{O}(k+1)}|/|\boldsymbol{f}_{\boldsymbol{b}}^{\mathrm{O}(k)}| \ll 1$ for $b^*/b \ll 1$ with positive integer k. This expansion is reasonable for observation times $\Delta t \ll \tau_\mathrm{C}$, because most of the tracer displacement at this timescale originates from such scattering events with high probability.

The inner layer FSF $\boldsymbol{f}_{\boldsymbol{b}}^\mathrm{I}(t)$ is set to be zero as an approximation, as there is no interaction force within the tracer core. This approximation is not exact but is expected valid to study the power-law tail of the displacement statistics, since the inner layer mainly contributes to the truncation of the power law. Moments, on the other hand, may be sensitive to the detail of the inner layer FSF. More refined approximations will be discussed in future publications.

Thus, we defined the FSF for the cases $|b| \le d$ and $|b| \gg b^*$. Within the spirit of boundary layer analysis, as a phenomenological approximation we connect these solutions as

$$\boldsymbol{f}_{\boldsymbol{b}}(t) \equiv \begin{cases} \boldsymbol{f}_{\boldsymbol{b}}^{\mathrm{O}(1)}(t) + \boldsymbol{f}_{\boldsymbol{b}}^{\mathrm{O}(2)}(t) & |b| > d \\ \boldsymbol{f}_{\boldsymbol{b}}^\mathrm{I}(t) & |b| \le d \end{cases}. \tag{S22}$$

To compute the tracer displacement statistics, we will focus on the projection along the x-direction $\boldsymbol{e}_x \equiv (1, 0, 0)$. The tracer stochastic dynamics in this direction is fully determined by the projected FSF $f_{\boldsymbol{b}}(t) \equiv \boldsymbol{e}_x \cdot \boldsymbol{f}_{\boldsymbol{b}}(t)$.

C. Asymptotic expansion of the outer layer force shape function

The asymptotic expansion of $\boldsymbol{f}_{\boldsymbol{b}}^\mathrm{O}$ for large impact parameters is obtained by first approximating the exact solution of Eq. (S18) up to a second order Picard iteration and, secondly, by Taylor expanding the second iterate in terms of the tracer displacement from its position $\boldsymbol{X}_0$ at the collision time $t = 0$. We denote $\boldsymbol{X}^{(0)} = \boldsymbol{X}_0, \boldsymbol{X}^{(1)}, \dots, \boldsymbol{X}^{(n)}$

successive approximations of the exact solution of Eq. (S18) obtained via Picard iteration. They satisfy the recursive relation:

$$\boldsymbol{X}^{(n+1)}(t) = \boldsymbol{X}_0 + \frac{1}{\Gamma}\int_0^t \boldsymbol{F}(\boldsymbol{x}_1(t) - \boldsymbol{X}^{(n)}(t), \boldsymbol{n}_1)\,\mathrm{d}t'. \tag{S23}$$

Considering only the first and second iterations, we find

$$\boldsymbol{X}^{(1)}(t) = \boldsymbol{X}_0 + \frac{1}{\Gamma}\int_0^t \boldsymbol{F}(\boldsymbol{x}_1(t) - \boldsymbol{X}_0, \boldsymbol{n}_1)\,\mathrm{d}t', \tag{S24}$$

$$\boldsymbol{X}^{(2)}(t) = \boldsymbol{X}_0 + \frac{1}{\Gamma}\int_0^t \boldsymbol{F}(\boldsymbol{x}_1(t) - \boldsymbol{X}^{(1)}(t), \boldsymbol{n}_1)\,\mathrm{d}t'. \tag{S25}$$

Taking the time derivative of Eq. (S24) yields

$$\frac{\mathrm{d}\boldsymbol{X}^{(1)}(t)}{\mathrm{d}t} = \frac{1}{\Gamma}\boldsymbol{F}(\boldsymbol{x}_1(t) - \boldsymbol{X}_0, \boldsymbol{n}_1). \tag{S26}$$

After setting $\boldsymbol{X}_0 = (0,0,0)$, we obtain the first order contribution to the FSF, i.e., the term $\boldsymbol{f}_{\boldsymbol{b}}^{\mathrm{O}(1)}$ in Eq. (S21).

We then define the tracer displacement at first order $\Delta\boldsymbol{X}^{(1)}(t) = \boldsymbol{X}^{(1)}(t) - \boldsymbol{X}_0$. Upon rescaling length- and timescales by b^* and τ_{H}, respectively, by introducing dimensionless variables

$$x \equiv \frac{b}{b^*}, \qquad y \equiv \frac{t}{\tau_{\mathrm{H}}}, \tag{S27}$$

the solution is given by

$$\Delta\boldsymbol{X}^{(1)}(y) = \frac{p}{|p|}b^*\int_0^y \frac{1}{|x\boldsymbol{e}_b + y'\boldsymbol{n}_1 - \boldsymbol{X}_0|^2}\left[3\frac{(\boldsymbol{n}_i\cdot(x\boldsymbol{e}_b + y'\boldsymbol{n}_1 - \boldsymbol{X}_0))^2}{|x\boldsymbol{e}_b + y'\boldsymbol{n}_1 - \boldsymbol{X}_0|^2} - 1\right]\frac{x\boldsymbol{e}_b + y'\boldsymbol{n}_1 - \boldsymbol{X}_0}{|x\boldsymbol{e}_b + y'\boldsymbol{n}_1 - \boldsymbol{X}_0|}\,\mathrm{d}y'. \tag{S28}$$

Clearly, for large impact parameters $b/b^* \gg 1$, which is equivalent to $x \gg 1$, $|\Delta\boldsymbol{X}^{(1)}| \simeq 0$. This is ultimately a consequence of the long-range decay of the far-field hydrodynamic force. Therefore, the rhs of Eq. (S25) can be Taylor expanded as

$$\begin{aligned}\boldsymbol{X}^{(2)}(t) &= \boldsymbol{X}_0 + \frac{1}{\Gamma}\int_0^t \boldsymbol{F}(\boldsymbol{x}_1(t') - \boldsymbol{X}_0, \boldsymbol{n}_1)\,\mathrm{d}t' + \frac{1}{\Gamma}\int_0^t \Delta\boldsymbol{X}^{(1)}(t')\cdot\nabla_{\boldsymbol{X}}\boldsymbol{F}(\boldsymbol{x}_1(t') - \boldsymbol{X}_0, \boldsymbol{n}_1)\,\mathrm{d}t' \\ &= \boldsymbol{X}^{(1)}(t) + \frac{1}{\Gamma}\int_0^t \Delta\boldsymbol{X}^{(1)}(t')\cdot\nabla_{\boldsymbol{X}}\boldsymbol{F}(\boldsymbol{x}_1(t') - \boldsymbol{X}_0, \boldsymbol{n}_1)\,\mathrm{d}t'.\end{aligned} \tag{S29}$$

Taking its time derivative, we then obtain:

$$\frac{\mathrm{d}}{\mathrm{d}t}[\boldsymbol{X}^{(2)}(t) - \boldsymbol{X}^{(1)}(t)] = \frac{1}{\Gamma}\Delta\boldsymbol{X}^{(1)}(t)\cdot\nabla_{\boldsymbol{X}}\boldsymbol{F}(\boldsymbol{x}_1(t) - \boldsymbol{X}_0, \boldsymbol{n}_1). \tag{S30}$$

As previously, setting $\boldsymbol{X}_0 = (0,0,0)$ yields the second order contribution to the FSF, i.e., the term $\boldsymbol{f}_{\boldsymbol{b}}^{\mathrm{O}(2)}$ in Eq. (S21). In summary, we derived the following equations:

$$\boldsymbol{f}_{\boldsymbol{b}}^{\mathrm{O}(1)}(t) = \boldsymbol{F}(\boldsymbol{x}_1(t), \boldsymbol{n}_1), \tag{S31}$$

$$\boldsymbol{f}_{\boldsymbol{b}}^{\mathrm{O}(2)}(t) = \boldsymbol{X}^{(1)}(t)\cdot\nabla_{\boldsymbol{X}}\boldsymbol{F}(\boldsymbol{x}_1(t), \boldsymbol{n}_1), \tag{S32}$$

where $\boldsymbol{X}^{(1)}(t) = \int_0^t \boldsymbol{F}(\boldsymbol{x}_1(t'), \boldsymbol{n}_1)\,\mathrm{d}t'$. These fully specify the asymptotic expansion of the outer layer FSF Eq. (S21).

D. Projected outer layer force shape function for the stresslet hydrodynamic force

Using Eqs. (S31, S32), we compute the FSF for the stresslet hydrodynamic force (2) projected in the direction $\boldsymbol{e}_x$. Here the x axis can be fixed arbitrarily if the x, y, z axes are fixed orthogonally, since this system is isotropic. Details of the calculation are presented in Section VI A. In the dimensionless variables (S27) this is given by

$$f_{\boldsymbol{b}}^{\mathrm{O}}(t) \equiv \Gamma v_{\mathrm{A}} f_{\boldsymbol{x}}^{\mathrm{O}}(y), \qquad f_{\boldsymbol{x}}^{\mathrm{O}}(y) \equiv g_1(x,y)\mathcal{A}(\theta,\phi,\phi') + g_2(x,y)\mathcal{B}(\theta,\phi,\phi'), \tag{S33}$$

where $\boldsymbol{x} \equiv (x, \theta, \phi, \phi')$ and we define the auxiliary functions g_1, g_2 as

$$g_1(x,y) \equiv \frac{1}{(x^2+y^2)^{5/2}} \left[\frac{p}{|p|} x(2y^2 - x^2) + \frac{3y(2y^2-3x^2)}{x^2+y^2} + \frac{xy(11x^2-10y^2)}{(x^2+y^2)^{3/2}} \right], \tag{S34}$$

$$g_2(x,y) \equiv \frac{1}{(x^2+y^2)^{5/2}} \left[\frac{p}{|p|} y(2y^2 - x^2) + \frac{x^4-10x^2y^2+4y^4}{x(x^2+y^2)} + \frac{-x^6+11x^4y^2+4x^2y^4-8y^6}{(x^2+y^2)^{5/2}} \right] \tag{S35}$$

and those dependent on the injection angles

$$\mathcal{A}(\theta, \phi, \phi') \equiv \sin\theta \cos\phi, \tag{S36}$$

$$\mathcal{B}(\theta, \phi, \phi') \equiv \cos\theta \cos\phi \cos\phi' - \sin\phi \sin\phi'. \tag{S37}$$

The two functions g_1 and g_2 constitute a base representation of the general solution $f^{\mathrm{O}}_{\boldsymbol{x}}(y)$, which can be obtained in full generality by their linear combinations weighted by the two functions $\mathcal{A}$ and $\mathcal{B}$ dependent on the injection angles. Due to their fundamental significance to understand the mathematical structure of the FSF, we plot g_1 and g_2 in Fig. 2b (main text). In addition, to assess the goodness of our analytical result, we arbitrarily select independent scattering events from the time series of the force exerted on the tracer by the active swimmers, which are obtained through numerical simulations of the microscopic model (1) (main text, Fig. 2a), and fit the extracted data by using Eqs. (S33-S37). The fit parameters are the characteristic parameter set of the scattering $\boldsymbol{b}$ and the scattering time τ. This latter parameter is necessary because the long-range nature of the hydrodynamic interactions in our system allows interaction events at any time finite t after initialization to be significant for the tracer displacement statistics. Two exemplary fits are presented in Fig. 2c (main text; black solid line) together with the corresponding simulation data (coloured markers). The fitting is performed by using non-linear least squares method, which yields the following results for the fit parameters: $\tau = 11726.35$, $b = 27.20$, $\theta = 2.14$, $\phi = 0.02$, $\phi' = 0.93$ (top panel); $\tau = 75849.77$, $b = 152.23$, $\theta = 0.68$, $\phi = 3.36$, $\phi' = 3.48$ (bottom panel). The agreement between the simulation data and the fit curves is very good, which thus supports the validity of our theoretical approximations and analytical formulas.

III. CHARACTERISTIC FUNCTIONAL OF THE COLOURED POISSON MODEL AND TRACER DISPLACEMENT STATISTICS

To study the displacement statistics of the tracer projected in the direction $\boldsymbol{e}_x$, we employ the characteristic functional method [39]. For the coloured Poisson noise $F \equiv \boldsymbol{e}_x \cdot \boldsymbol{F}$ (see Eq. (3) for its definition), the characteristic functional is given by

$$\log \chi[g(s)] = \log \left\langle e^{i \int_{-\infty}^{\infty} g(s) F(s)\, \mathrm{d}s} \right\rangle = \int_{-\infty}^{\infty} \mathrm{d}t \int \mathrm{d}\boldsymbol{b} \lambda(\boldsymbol{b}) \left[e^{i \int_{-\infty}^{\infty} g(s) f_{\boldsymbol{b}}(s-t)\, \mathrm{d}s} - 1 \right], \tag{S38}$$

where the FSF is prescribed as Eqs. (S22) and $\mathrm{d}\boldsymbol{b} \equiv |J_{\boldsymbol{b}}|\, \mathrm{d}b\, \mathrm{d}\theta\, \mathrm{d}\phi\, \mathrm{d}\phi'$ with $\lambda(\boldsymbol{b})|J_{\boldsymbol{b}}|$ as in Eq. (S15). The detailed derivation of Eq. (S38) is reported in Section VI B. Here we also consider the contribution of thermal fluctuations modelled by a three dimensional isotropic Brownian motion with variance $2k_{\mathrm{B}}\Gamma T$ in Eq. (3) with k_{B} the Boltzmann constant and T the temperature of the bath at zero concentration of active swimmers. The characteristic functional of the thermal noise is

$$\log \chi[g(s)] = \log \left\langle e^{i \int_{-\infty}^{\infty} g(s) \xi(s)\, \mathrm{d}s} \right\rangle = -k_{\mathrm{B}}\Gamma T \int_{-\infty}^{\infty} [g(t)]^2\, \mathrm{d}t. \tag{S39}$$

Using these results, the Fourier transform of the tracer displacement distribution $P_{\Delta t}(\Delta X)$ is easily obtained by setting $g(s) = (k/\Gamma)\Theta(\Delta t - s)\Theta(s)$ (here Θ is a Heaviside function defined by $\Theta(x) = 1$ for $x > 0$, $\Theta(x) = 1/2$ for $x = 0$, and $\Theta(x) = 0$ for $x < 0$). This yields

$$\log \widehat{P}_{\Delta t}(k) = \int_{-\infty}^{\infty} \mathrm{d}t' \int \mathrm{d}\boldsymbol{b} \lambda(\boldsymbol{b}) \left[\exp\left(i \frac{k}{\Gamma} \int_0^{\Delta t} f_{\boldsymbol{b}}(s-t')\, \mathrm{d}s \right) - 1 \right] - k^2 D_0 \Delta t \tag{S40}$$

with $D_0 \equiv k_{\mathrm{B}}T/\Gamma$ the thermal diffusion coefficient.

The power-law scaling of the tails of the tracer displacement distribution is studied by asymptotically expanding this formula for null truncation $d \approx 0$ (see Sections VI D, VI E). The Gaussian scaling in the CLT regime is instead

obtained for finite truncation (see Section VI F). Thus, we obtain asymptotic relations for the characteristic function

$$\log \widehat{P}_{\Delta t}(k) \approx \begin{cases} -C_{\rm H}\Delta t^{3/2}|k|^{3/2} & (\Delta t \ll \tau_{\rm H}) \\ -C_{\rm S}\Delta t|k|^{2/3} & (\tau_{\rm H} \ll \Delta t \ll \tau_{\rm C}) \\ -\sigma^2 \Delta t\, k^2/2 & (\tau_{\rm C} \ll \Delta t) \end{cases}, \tag{S41}$$

with coefficients $C_{\rm H} \equiv 0.96\rho(|p|/\Gamma)^{3/2}$, $C_{\rm S} \equiv 0.21\rho v_{\rm A}[|p|/(\Gamma v_{\rm A})]^{4/3}$ and $\sigma^2 \equiv 2D_0 + \sigma_a^2$ with the contribution due to the active swimmers $\sigma_a^2 \equiv 0.02(\rho v_{\rm A}/d^4)[|p|/(\Gamma v_{\rm A})]^4$. Here the Markovian approximation implies $f_{\boldsymbol{b}}(s-t') \approx C_{\rm M}(\boldsymbol{b})\delta(s-t')$ with $C_{\rm M}(\boldsymbol{b}) \equiv \int_{-\infty}^{\infty} {\rm d}t f_{\boldsymbol{b}}(t) = -\pi p^2 \mathcal{B}(\theta,\phi,\phi')/(16\Gamma v_{\rm A}^2 b^3)$ for $\tau_{\rm H} \ll \Delta t \ll \tau_{\rm C}$. These relations imply Eq. (4).

A. Mean square displacement of the coloured Poisson model

Because the tracer is initially at position $\boldsymbol{X}_0 = (0,0,0)$, the MSD is the second moment of its displacement distribution. For simplicity, we restrict our calculation to the motion along the x-axis. Employing the well known formula for the general n-th cumulant of the displacement statistics [16]

$$\langle \Delta X^n \rangle_{\rm c} = \left. \frac{{\rm d}^n}{{\rm d}(ik)^n} \log \widehat{P}_{\Delta t}(k) \right|_{k=0}, \tag{S42}$$

we find straightforwardly that $\langle \Delta X \rangle_{\rm c} = 0$ (because $\int_0^{2\pi} {\rm d}\theta f_{\boldsymbol{b}} = 0$), such that $\langle \Delta X^2 \rangle = \langle \Delta X^2 \rangle_c$. Therefore, the MSD is equal to the second order cumulant $\langle \Delta X^2 \rangle_{\rm c}$. Setting $n = 2$ in Eq. (S42), we obtain

$$\mathrm{MSD}(\Delta t) = \frac{1}{\Gamma^2} \int_{-\infty}^{\infty} {\rm d}t \int {\rm d}\boldsymbol{b} \lambda(\boldsymbol{b}) \prod_{i=1}^{2} \int_0^{\Delta t} {\rm d}s_i f_{\boldsymbol{b}}(s_i - t) + 2D_0 \Delta t. \tag{S43}$$

Applying similar arguments as for the displacement PDF, and neglecting at first the thermal contribution, we obtain the asymptotic relations (see Section VI G)

$$\mathrm{MSD}(\Delta t) \approx \begin{cases} D_{\rm H}\Delta t^2 & (\Delta t \ll \tau_{\rm H}) \\ D_{\rm S}\Delta t & (\tau_{\rm H} \ll \Delta t) \end{cases}, \tag{S44}$$

where the coefficients are defined as $D_{\rm H} \propto \rho v_{\rm A}^2 [|p|/(\Gamma v_{\rm A})]^{3/2}$ and $D_{\rm S} \propto \rho v_{\rm A} \left[|p|/(\Gamma v_{\rm A})\right]^2$. Adding the thermal noise, we see that the MSD is shifted by the time-dependent factor $2D_0\Delta t$. This term breaks the data collapse of the MSD upon rescaling by $1/\rho b^{*5}$ (see main text) because the parameter D_0, being independent on ρ and b^*, remains unchanged upon such rescaling.

B. Non-Gaussian parameter of the coloured Poisson model

The non-Gaussian parameter (NGP) of the tracer displacement distribution is defined as

$$\mathrm{NGP}(\Delta t) \equiv \frac{\langle \Delta X^4 \rangle}{3\langle \Delta X^2 \rangle^2} - 1, \tag{S45}$$

where the second moment of the displacement statistics has already been calculated and the fourth one is similarly computed by using Eq. (S42). In particular, because the first cumulant is null, we find $\langle \Delta X^4 \rangle = \langle \Delta X^4 \rangle_c + 3\langle \Delta X^2 \rangle_c^2$. Therefore,

$$\mathrm{NGP}(\Delta t) \equiv \frac{\langle \Delta X^4 \rangle_c}{3\langle \Delta X^2 \rangle_c^2}. \tag{S46}$$

As in the previous sections, and neglecting at first the thermal contribution, we obtain the relations (see Section VI H)

$$\mathrm{NGP}(\Delta t) \approx \begin{cases} B_{\rm H} & (\Delta t \ll \tau_{\rm H}) \\ B_{\rm S}/\Delta t & (\tau_{\rm H} \ll \Delta t) \end{cases}, \tag{S47}$$

where the coefficients are defined as $B_{\rm H} \propto [|p|/(\Gamma v_{\rm A})]^{-3/2}\,\rho^{-1}$ and $B_{\rm S} \propto (\rho v_{\rm A})^{-1}[|p|/(\Gamma v_{\rm A})]^{-1}$.

Adding now the thermal contribution, which has null fourth cumulant, we obtain

$$\mathrm{NGP}(\Delta t) \approx \begin{cases} B_{\rm H}/(1+2\tilde{D}_0^{(\rm H)}/\Delta t)^2 & (\Delta t \ll \tau_{\rm H}) \\ B_{\rm S}/[(1+2\tilde{D}_0^{(\rm S)})^2 \Delta t] & (\tau_{\rm H} \ll \Delta t) \end{cases}, \tag{S48}$$

with the rescaled thermal coefficients $\tilde{D}_0^{(\rm H)} \equiv D_0(\rho v_{\rm A}^2)^{-1}[|p|/(\Gamma v_{\rm A})]^{-3/2}/D_{\rm H}$ and $\tilde{D}_0^{(\rm S)} \equiv D_0(\rho v_{\rm A})^{-1}[|p|/(\Gamma v_{\rm A})]^{-2}/D_{\rm S}$. Therefore, we observe that (a) the scaling behaviour $\propto \Delta t^{-1}$ characteristic of the scattering regime is robust against the addition of the thermal noise and (b), similarly to the MSD, the data collapse upon rescaling by ρb^{*3} (see main text) is no longer valid, because the thermal diffusion coefficient D_0 is independent on these parameters, such that the terms depending on D_0 remain unchanged upon the rescaling.

C. Derivation of the scaling exponents for the tracer displacement statistics for general D-dimensional active flows

The derivation of the Poisson intensity $\lambda(\boldsymbol{b})$ presented in Sec. II A can be extended straightforwardly in D-dimensions, thus yielding the relation

$$\lambda(\boldsymbol{b})|J_{\boldsymbol{b}}| = b^{D-2} w(\boldsymbol{\Omega}) \tag{S49}$$

with the auxiliary function w specifying the angular structure.

For short timescales $\Delta t \ll \tau_{\rm H}$, the tracer displacement statistics can thus be written as (here we neglect the thermal contribution)

$$\log \widehat{P}_{\Delta t}(k) = \int_{-\infty}^{\infty} \mathrm{d}t \int_{d}^{\infty} \mathrm{d}b\, b^{D-2} \int \mathrm{d}\boldsymbol{\Omega}\, w(\boldsymbol{\Omega}) \left[-1 + e^{\,i\frac{k}{\Gamma}\Delta t f_{\boldsymbol{b}}(t)}\right]. \tag{S50}$$

Let us consider a general hydrodynamic force $\boldsymbol{F}(\boldsymbol{r}_i, \boldsymbol{n}_i) \propto \boldsymbol{r}_i^{-n_{\rm H}}$ (we recall that $\boldsymbol{r}_i = \boldsymbol{x}_i - \boldsymbol{X}$ and $\boldsymbol{n}_i$ is the direction of motion of the active swimmer). With these assumptions, the force shape function can be specified as

$$f_{\boldsymbol{b}}^{\rm O}(t) = |p| b^{*\,-n_{\rm H}} f_{\boldsymbol{x}}^{\rm O}(y) \tag{S51}$$

with $\boldsymbol{x} \equiv (x, \boldsymbol{\Omega})$, the dimensionless variables x, y defined in Eq. (S27) and the auxiliary function

$$f_{\boldsymbol{x}}^{\rm O}(y) = x^{-n_{\rm H}} f_{\boldsymbol{\Omega}}^{\rm O}(z). \tag{S52}$$

Introducing the variable $z = y/x$ allows to factorize out the scaling dependence in x of this function, which determines the scaling exponents $\alpha_{\rm H}$. In fact, rewriting Eq. (S50) in the variables (x, z) we obtain

$$\log \widehat{P}_{\Delta t}(k) = b^{*\,D-1}\tau_{\rm H} \int_{-\infty}^{\infty} \mathrm{d}z \int_{d/b^*}^{\infty} \mathrm{d}x\, x^{D-1} \int \mathrm{d}\boldsymbol{\Omega}\, w(\boldsymbol{\Omega}) \left[-1 + e^{\,i\widetilde{k}\,\Delta y\, b^{*\,2-n_{\rm H}} x^{-n_{\rm H}} f_{\boldsymbol{\Omega}}^{\rm O}(z)}\right] \tag{S53}$$

with $\widetilde{k} = kb^*$. The tail behaviour is obtained by considering $d \approx 0$. Therefore,

$$\log \widehat{P}_{\Delta t}(k) = b^{*\,D-1}\tau_{\rm H} \int_{-\infty}^{\infty} \mathrm{d}z \int_{0}^{\infty} \mathrm{d}x\, x^{D-1} \int \mathrm{d}\boldsymbol{\Omega}\, w(\boldsymbol{\Omega}) \left[-1 + e^{\,i\widetilde{k}\,\Delta y\, b^{*\,2-n_{\rm H}} x^{-n_{\rm H}} f_{\boldsymbol{\Omega}}^{\rm O}(z)}\right]. \tag{S54}$$

Changing variables as $x' \equiv x[\widetilde{k}\,\Delta y\, b^{*\,2-n_{\rm H}}]^{-1/n_{\rm H}}$ we obtain

$$\log \widehat{P}_{\Delta t}(k) = b^{*\,D-1}\tau_{\rm H}[\widetilde{k}\,\Delta y\, b^{*\,2-n_{\rm H}}]^{D/n_{\rm H}} \int_{-\infty}^{\infty} \mathrm{d}z \int_{0}^{\infty} \mathrm{d}x'\, x'^{\,D-1} \int \mathrm{d}\boldsymbol{\Omega}\, w(\boldsymbol{\Omega}) \left[-1 + e^{\,ix'^{\,-n_{\rm H}} f_{\boldsymbol{\Omega}}^{\rm O}(z)}\right]. \tag{S55}$$

Therefore, we obtain the asymptotic formula

$$\log \widehat{P}_{\Delta t}(k) \approx -\Upsilon_{\rm H}\, b^{*\,-1+3D/n_{\rm H}}\, \tau_{\rm H}^{1-D/n_{\rm H}} \Delta t^{D/n_{\rm H}} |k|^{D/n_{\rm H}} \longrightarrow P_{\Delta t}(|\Delta X|) \propto |\Delta X|^{-(1+D/n_{\rm H})} \tag{S56}$$

with the numerical coefficient

$$\Upsilon_{\rm H} = \int_{-\infty}^{\infty} \mathrm{d}z \int_{0}^{\infty} \mathrm{d}x'\, x'^{\,D-1} \int \mathrm{d}\boldsymbol{\Omega}\, w(\boldsymbol{\Omega}) \left[-1 + e^{\,ix'^{\,-n_{\rm H}} f_{\boldsymbol{\Omega}}^{\rm O}(z)}\right]. \tag{S57}$$

For intermediate timescales $\tau_{\rm H} \ll \Delta t \ll \tau_{\rm S}$, instead, we obtain

$$\log \widehat{P}_{\Delta t}(k) = \Delta t \int_d^\infty {\rm d}b\, b^{D-2} \int {\rm d}\mathbf{\Omega}\, w(\mathbf{\Omega}) \left[-1 + e^{\,i\frac{k}{\Gamma} y(\boldsymbol{b})}\right] \tag{S58}$$

with the total displacement of the tracer

$$y(\boldsymbol{b}) = |p|\, \tau_{\rm H}\, b^{*\,-n_{\rm S}} x^{-n_{\rm S}} y'(\mathbf{\Omega}). \tag{S59}$$

Equation (S58) in dimensionless coordinates therefore becomes

$$\log \widehat{P}_{\Delta t}(k) = \tau_{\rm H} b^{*\,D-1} \Delta y \int_{d/b^*}^\infty {\rm d}x\, x^{D-2} \int {\rm d}\mathbf{\Omega}\, w(\mathbf{\Omega}) \left[-1 + e^{\,i\,k\,b^{*\,3-n_{\rm S}} x^{-n_{\rm S}} y'(\mathbf{\Omega})}\right]. \tag{S60}$$

As previously, the tail behaviour is obtained by assuming $d \approx 0$. Thus, changing variables as $x' \equiv x(k\, b^{*\,3-n_{\rm S}})^{-1/n_{\rm S}}$, we obtain

$$\log \widehat{P}_{\Delta t}(k) = \tau_{\rm H} \Delta y b^{*\,3(D-1)/n_{\rm S}}\, k^{(D-1)/n_{\rm S}} \int_{d/b^*}^\infty {\rm d}x'\, x'^{\,D-2} \int {\rm d}\mathbf{\Omega}\, w(\mathbf{\Omega}) \left[-1 + e^{\,i\,x'^{\,-n_{\rm S}} y'(\mathbf{\Omega})}\right]. \tag{S61}$$

Therefore, we obtain the asymptotic formula

$$\log \widehat{P}_{\Delta t}(k) \approx -\Upsilon_{\rm S}\, b^{*\,3(D-1)/n_{\rm S}}\, \Delta t |k|^{(D-1)/n_{\rm S}} \longrightarrow P_{\Delta t}(|\Delta X|) \propto |\Delta X|^{-[1+(D-1)/n_{\rm S}]} \tag{S62}$$

with the numerical coefficient

$$\Upsilon_{\rm S} = \int_0^\infty {\rm d}x'\, x'^{\,D-2} \int {\rm d}\mathbf{\Omega}\, w(\mathbf{\Omega}) \left[-1 + e^{\,ix'^{\,-n_{\rm S}} y'(\mathbf{\Omega})}\right]. \tag{S63}$$

IV. A BRIEF REVIEW ON LÉVY PROCESSES

The Lévy flight is part of a much larger class of processes known in the mathematical literature as "Lévy processes" [38, 40, 41]. In the following we provide a brief introduction to Lévy processes and provide the precise definition of the Lévy flight further below. The stochastic process Y with initial condition $Y(0) = y_0$ is a Lévy process if (i) $y_0 = 0$ almost surely, (ii) Y has independent increments, i.e., $\forall\, n \geq 2$ and for each partition $0 \leq t_0 < t_1 < \ldots < t_n \leq t$ the random variables $\{Y(t_j) - Y(t_{j-1})\}$ for $j = 1, \ldots, n$ are independent, (iii) Y has stationary increments, meaning that for all $0 \leq t_1 < t_2 \leq t$ the random variable $Y(t_2) - Y(t_1)$ has the same distribution as $Y(t_2 - t_1)$ and (iv) Y has càdlàg (right-continuous with left limits) trajectories. Restricting the conditions (ii), (iv) by assuming Gaussian distributed increments and continuous trajectories respectively recovers ordinary Brownian motion. As a consequence of properties (ii) and (iii), Y can be written as an arbitrary sum of different independent and identically distributed random variables X, i.e., Y is infinitely divisible. This result is particularly important as it allows to specify the characteristic function of the process Y in terms of the Lévy-Khintchin formula for infinitely divisible random variables. In details

$$\langle e^{ikY(t)} \rangle = e^{\,it\eta(k)}, \qquad\qquad \eta(k) = ibk - \frac{\sigma}{2}k^2 + \int_{\mathbb{R}/\{0\}} [e^{\,iky} - 1 - iky \mathbf{1}_{|y|<1}(y)]\, \nu({\rm d}y) \tag{S64}$$

with real parameters b, $\sigma \geq 0$, the indicator function $\mathbf{1}_{\rm A}$ on the set A, which is defined as $\mathbf{1}_A(y) = 1$ for $y \in A$ or $\mathbf{1}_A(y) = 0$ otherwise, and the Lévy (probability) measure ν on $\mathbb{R}/\{0\}$ satisfying $\int_{\mathbb{R}/\{0\}} {\rm Max}(|y|^2, 1)\, \nu({\rm d}y) < \infty$. η is called the *Lévy symbol* of the process Y.

Important examples of Lévy processes are (a) Brownian motion (as already mentioned) for which $\eta(k) = ibk - \sigma^2 k^2/2$; (b) the Poisson Process with rate λ that is obtained by setting $b = \sigma = 0$ and $\nu = \lambda\delta(y-1)\,{\rm d}y$ yielding $\eta(k) = \lambda\,(e^{\,i\,k} - 1)$; and (c) the Compound Poisson Process. A Compound Poisson process on the interval $[0, t]$ is defined by sampling $N(t)$ independent random variables $\{\nu_i\}$ distributed with some prescribed law $\nu({\rm d}y)$, where $N(t)$ is Poisson distributed $\forall\, t > 0$. It is thus a sequence of jumps of random amplitudes occurring at exponentially distributed random intervals Δt with law $P(\Delta t) = e^{\,-\lambda \Delta t}$ (here the frequency λ is the inverse of the mean time between the jumps). Its Lévy symbol is (we set $b = \sigma = 0$)

$$\eta(k) = \lambda \int_{-\infty}^\infty (e^{\,iky} - 1)\nu({\rm d}y). \tag{S65}$$

Another important group is that of (d) stable processes, also known as the Lévy flights, which are Lévy processes with increments sampled from a stable distribution. The stable distribution has the power-law tail, and thus the stable process is a generalization of the random walks model with power-law jump size distribution for continuous time. We refer to [42] for further details.

Let us now interpret the projected stochastic dynamics of the tracer $X \equiv \boldsymbol{e}_x \cdot \boldsymbol{X}$ as described by the coloured Poisson model (3) to the theory just outlined. By comparing its characteristic function (S40) (here we neglect the thermal Brownian contribution) and the general formula (S64) (which is also valid in higher dimensions), we understand that this dynamics do not belong to the class of Lévy processes in general terms. In fact, the explicit dependence on the timescale Δt of the jump amplitudes, which is fundamentally due to the long-range decaying hydrodynamic interaction, easily breaks properties (ii) and (iii) outlined above. Nevertheless, an equivalent description as Lévy process is recovered when this dependence is negligible because Δt is large enough that the interaction can be resolved as an instantaneous shot within the effective picture of the Markovian approximation (scattering regime, see schematic in Fig. S3c and Eq. (S112)). In this case, in particular, the dynamics predicted by the model (3) is equivalent to a compound Poisson process with power-law distributed jump sizes. As a consequence of the infinite intensity of the process, which causes an accumulation of an infinite number of such jumps, this process becomes effectively described by the Lévy flight model endowed with a finite cutoff (see Section II A).

V. EXPERIMENTAL VALIDATION: POWER-LAW VS. EXPONENTIAL TAILS

Despite the vast literature on experimental studies of tracer motion in bacterial suspensions, some confusion still persists about the type of scaling behaviour that the tails of its displacement statistics exhibit. While some authors find clear evidence for power-law scaling [6, 10, 23], others claim to observe an exponential instead [4, 9]. Our stochastic model of the tracer dynamics resolves this issue by predicting power-law scaling behaviour (see Eq. (S41)), which is fundamentally due to the long-range hydrodynamic swimmer-tracer interactions. This is shown to be valid in the main text for the displacement distribution (Fig. 3a). In Fig. S5, we clarify how this issue could be due to an insufficient sampling of the distribution tails. In fact, our data could also be well fitted by a sum of a Gaussian and an exponential function (dashed lines), if we restrict to about one/two orders of magnitude from the onset of the bulk of the distribution (see the plateaus). The power-law scaling becomes clear if all the data are used for the fit (solid lines). This discussion should serve as a suggestion that more refined experimental protocols need to be developed in order to improve the statistics of tracer displacements, and thus obtain the correct scaling behaviour of its tails.

VI. TECHNICAL CALCULATIONS

A. Derivation of the outer layer force shape function for the stresslet hydrodynamic force

We consider the setup depicted in Fig. S6a, which is obtained by rotating that of Fig. 1b with the rotation matrix

$$\mathcal{M}(\theta,\phi) \equiv \begin{pmatrix} \sin\theta & 0 & \cos\theta \\ 0 & 1 & 0 \\ -\cos\theta & 0 & \sin\theta \end{pmatrix} \begin{pmatrix} \cos\phi & \sin\phi & 0 \\ -\sin\phi & \cos\phi & 0 \\ 0 & 0 & 1 \end{pmatrix}. \tag{S66}$$

Thus, $\boldsymbol{f}_{\boldsymbol{b}}^{\mathrm{O}}$ is obtained by applying the inverse matrix

$$\mathcal{R}(\theta,\phi) \equiv \mathcal{M}^{-1}(\theta,\phi) = \begin{pmatrix} \cos\phi & -\sin\phi & 0 \\ \sin\phi & \cos\phi & 0 \\ 0 & 0 & 1 \end{pmatrix} \begin{pmatrix} \sin\theta & 0 & -\cos\theta \\ 0 & 1 & 0 \\ \cos\theta & 0 & \sin\theta \end{pmatrix} \tag{S67}$$

to the FSF obtained in this specific configuration. We assume the initial condition for the tracer $\boldsymbol{X}_0 = (0,0,0)$ and denote the position and direction of motion of the active particle as $\boldsymbol{x}$, $\boldsymbol{n}$ respectively. This initial condition is selected to simplify the apparent calculation. However, the generality of our setup is not lost under this assumption, since only the relative position is relevant for two-body scattering problems between the tracer and swimmer. For the setup specified, $\boldsymbol{n} = (0, \sin\phi', -\cos\phi')$ and the trajectory of the active particle is $\boldsymbol{x}(t) = (b, v_{\mathrm{A}} t \sin\phi', -v_{\mathrm{A}} t \cos\phi')$. Consequently, we find: $\boldsymbol{n} \cdot (\boldsymbol{x}(t) - \boldsymbol{X}_0) = v_{\mathrm{A}} t$ and $|\boldsymbol{x}(t) - \boldsymbol{X}_0| = \sqrt{b^2 + v_{\mathrm{A}}^2 t^2}$. Substituting them in Eq. (2) yields

$$\boldsymbol{F}(\boldsymbol{x}(t) - \boldsymbol{X}_0, t) = \frac{p}{(b^2 + v_{\mathrm{A}}^2 t^2)^{3/2}} \left(\frac{3 v_{\mathrm{A}}^2 t^2}{b^2 + v_{\mathrm{A}}^2 t^2} - 1 \right) \begin{pmatrix} b \\ v_{\mathrm{A}} t \sin\phi' \\ -v_{\mathrm{A}} t \cos\phi' \end{pmatrix}. \tag{S68}$$

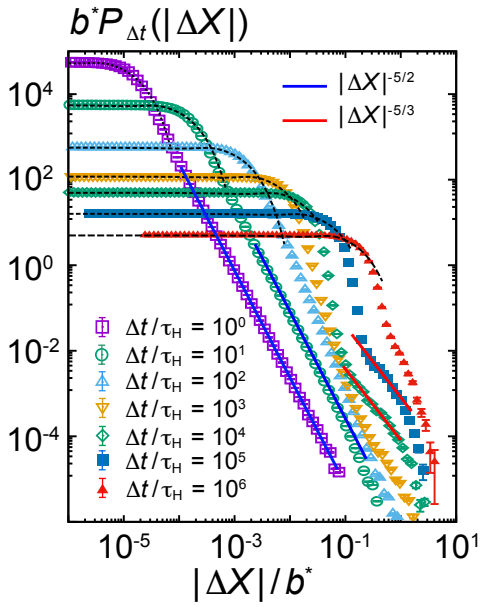

FIG. S5: Tracer displacement distribution $P_{\Delta t}(|\Delta X|)$ obtained from numerical simulations of the model (1). The asymptotic scaling behaviour of the tails predicted by Eq. (S41) is clearly confirmed (solid lines). Nevertheless, we show that our data are also well fitted by employing a linear superposition of a Gaussian and an exponential function (dashed lines), if the analysis is not pushed far into the tails (about up to two orders of magnitude from the onset of the plateau head of the distribution). Error bars denote ±1 s.e.m..

Thus, the FSF at first perturbation order is given by

$$\boldsymbol{f}_{\boldsymbol{b}}^{O(1)}(t) \equiv [\mathcal{R}(\theta,\phi)\boldsymbol{F}] = \frac{p}{(b^2+v_{\rm A}^2t^2)^{3/2}}\left(\frac{3v_{\rm A}^2t^2}{b^2+v_{\rm A}^2t^2}-1\right)\begin{pmatrix}(b\sin\theta+v_{\rm A}t\cos\theta\cos\phi')\cos\phi - v_{\rm A}t\sin\phi\sin\phi'\\(b\sin\theta+v_{\rm A}t\cos\theta\cos\phi')\sin\phi + v_{\rm A}t\cos\phi\sin\phi'\\ b\cos\theta - v_{\rm A}t\sin\theta\cos\phi'\end{pmatrix}. \quad \text{(S69)}$$

Its projection along the direction $\boldsymbol{e}_x$ is then

$$f_{\boldsymbol{b}}^{O(1)}(t) = \frac{p}{(b^2+v_{\rm A}^2t^2)^{3/2}}\left(\frac{3v_{\rm A}^2t^2}{b^2+v_{\rm A}^2t^2}-1\right)[(b\sin\theta+v_{\rm A}t\cos\theta\cos\phi')\cos\phi - v_{\rm A}t\sin\phi\sin\phi']. \quad \text{(S70)}$$

Its time integral over $(-\infty,\infty)$, which determines the total displacement of the tracer during the scattering event, is null in agreement with previous studies [18]. In fact, we can check that

$$\int_{-\infty}^{\infty}\frac{v_{\rm A}t}{(b^2+v_{\rm A}^2t^2)^{3/2}}\left(\frac{3v_{\rm A}^2t^2}{b^2+v_{\rm A}^2t^2}-1\right)\mathrm{d}t = 0, \quad \text{(S71a)}$$

$$\int_{-\infty}^{\infty}\frac{b}{(b^2+v_{\rm A}^2t^2)^{3/2}}\left(\frac{3v_{\rm A}^2t^2}{b^2+v_{\rm A}^2t^2}-1\right)\mathrm{d}t = 0. \quad \text{(S71b)}$$

By time integration of Eq. (S68) we obtain the trajectory of the tracer after the first Picard iteration:

$$\boldsymbol{X}^{(1)}(t) = \frac{p}{\Gamma v_{\rm A}}\left[\frac{1}{b}\begin{pmatrix}0\\\sin\phi'\\-\cos\phi'\end{pmatrix} - \frac{1}{(b^2+v_{\rm A}^2t^2)^{3/2}}\begin{pmatrix}bv_{\rm A}t\\(b^2+2v_{\rm A}^2t^2)\sin\phi'\\-(b^2+2v_{\rm A}^2t^2)\cos\phi'\end{pmatrix}\right]. \quad \text{(S72)}$$

An exemplary plot of this trajectory is presented in Fig. S6b, where we plot the function $\boldsymbol{X}^{(1)}(t)$ for $t\in[-T,T]$ for $p=1$, $\Gamma=1$, $b=1$, $v_{\rm A}=1$. At this order of approximation, the tracer moves along a closed triangular trajectory during the scattering event for $T\to\infty$ [18].

To compute the second order we need $\nabla_{\boldsymbol{X}}\boldsymbol{F}$, which is specified by the following equations ($\boldsymbol{r}\equiv\boldsymbol{x}-\boldsymbol{X}$, $r\equiv|\boldsymbol{r}|$; numeric subscripts {1,2,3} denote the components along the axis {x,y,z} respectively):

$$\frac{\partial}{\partial X_j}F_j(\boldsymbol{r},t) = \frac{p}{r^3}\left[1-3\frac{r_j^2}{r^2}-3\frac{(\boldsymbol{n}\cdot\boldsymbol{r})(\boldsymbol{n}\cdot\boldsymbol{r}+2n_jr_j)}{r^2}+15\frac{r_j^2(\boldsymbol{n}\cdot\boldsymbol{r})^2}{r^4}\right], \quad \text{(S73)}$$

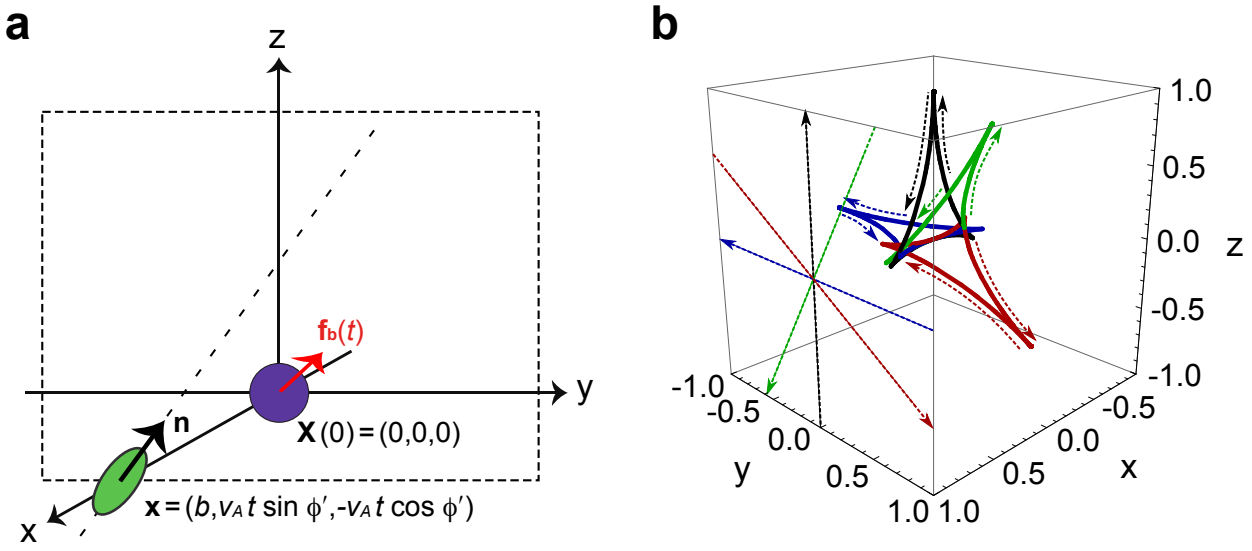

FIG. S6: (a) Schematic representation of the scattering event between active and passive particles employed to compute the force shape function. The motion of the active particle is restricted to a plane parallel to zy. (b) Exemplary triangular shaped loop-trajectories of the tracer during the scattering event after the first Picard iteration for different ϕ' (see Eq. (S72)). The trajectory of the active particles is also plotted (dashed straight lines). Parameters are $p = 1$, $\Gamma = 1$, $b = 1$, $v_A = 1$.

$$\frac{\partial}{\partial X_l} F_j(\boldsymbol{r}, t) = \frac{p}{r^5}\left[r_l r_j\left(15\frac{(\boldsymbol{n}\cdot\boldsymbol{r})^2}{r^2} - 3\right) - 6 n_l r_j (\boldsymbol{n}\cdot\boldsymbol{r})\right] \qquad (l \neq j). \tag{S74}$$

Further substituting $\boldsymbol{x}$ and $\boldsymbol{X}_0$, we obtain:

$$\frac{\partial}{\partial X_1} F_1(\boldsymbol{x}-\boldsymbol{X}_0, t) = \frac{p}{(b^2+v_A^2t^2)^{3/2}}\left[15\frac{b^2v_A^2t^2}{(b^2+v_A^2t^2)^2} - 2\right], \tag{S75a}$$

$$\frac{\partial}{\partial X_2} F_2(\boldsymbol{x}-\boldsymbol{X}_0, t) = \frac{p}{(b^2+v_A^2t^2)^{3/2}}\left[1 - 3(1+3\sin^2\phi')\frac{v_A^2t^2}{b^2+v_A^2t^2} + 15\sin^2\phi'\frac{v_A^4t^4}{(b^2+v_A^2t^2)^2}\right], \tag{S75b}$$

$$\frac{\partial}{\partial X_3} F_3(\boldsymbol{x}-\boldsymbol{X}_0, t) = \frac{p}{(b^2+v_A^2t^2)^{3/2}}\left[1 - 3(1+3\cos^2\phi')\frac{v_A^2t^2}{b^2+v_A^2t^2} + 15\cos^2\phi'\frac{v_A^4t^4}{(b^2+v_A^2t^2)^2}\right], \tag{S75c}$$

$$\frac{\partial}{\partial X_1} F_2(\boldsymbol{x}-\boldsymbol{X}_0, t) = \frac{3p(bv_At)\sin\phi'}{(b^2+v_A^2t^2)^{5/2}}\left(5\frac{v_A^2t^2}{b^2+v_A^2t^2} - 1\right) \tag{S75d}$$

$$\frac{\partial}{\partial X_1} F_3(\boldsymbol{x}-\boldsymbol{X}_0, t) = \frac{3p(bv_At)\cos\phi'}{(b^2+v_A^2t^2)^{5/2}}\left(1 - 5\frac{v_A^2t^2}{b^2+v_A^2t^2}\right), \tag{S75e}$$

$$\frac{\partial}{\partial X_2} F_1(\boldsymbol{x}-\boldsymbol{X}_0, t) = \frac{3p(bv_At)\sin\phi'}{(b^2+v_A^2t^2)^{5/2}}\left(5\frac{v_A^2t^2}{b^2+v_A^2t^2} - 3\right), \tag{S75f}$$

$$\frac{\partial}{\partial X_3} F_1(\boldsymbol{x}-\boldsymbol{X}_0, t) = \frac{3p(bv_At)\cos\phi'}{(b^2+v_A^2t^2)^{5/2}}\left(3 - 5\frac{v_A^2t^2}{b^2+v_A^2t^2}\right), \tag{S75g}$$

$$\frac{\partial}{\partial X_2} F_3(\boldsymbol{x}-\boldsymbol{X}_0, t) = \frac{\partial}{\partial X_3} F_2(\boldsymbol{x}_1-\boldsymbol{X}_0, t) = \frac{3p(v_A^2t^2)\cos\phi'\sin\phi'}{(b^2+v_A^2t^2)^{5/2}}\left(3 - 5\frac{v_A^2t^2}{b^2+v_A^2t^2}\right). \tag{S75h}$$

Substituting Eqs. (S72, S75) into Eq. (S32), we obtain:

$$\boldsymbol{X}^{(1)}\cdot\nabla_{\boldsymbol{X}} F_1 = \frac{p^2}{\Gamma v_A}\frac{1}{(b^2+v_A^2t^2)^{5/2}}\left[\frac{3v_At(2v_A^2t^2-3b^2)}{b^2+v_A^2t^2} + \frac{bv_At(11b^2-10v_A^2t^2)}{(b^2+v_A^2t^2)^{3/2}}\right], \tag{S76}$$

$$\boldsymbol{X}^{(1)}\cdot\nabla_{\boldsymbol{X}} F_2 = \frac{p^2}{\Gamma v_A}\frac{\sin\phi'}{(b^2+v_A^2t^2)^{5/2}}\left[\frac{b^4-10b^2v_A^2t^2+4v_A^4t^4}{b(b^2+v_A^2t^2)} + \frac{-b^6+11b^4v_A^2t^2+4b^2v_A^4t^4-8v_A^6t^6}{(b^2+v_A^2t^2)^{5/2}}\right], \tag{S77}$$

$$\boldsymbol{X}^{(1)}\cdot\nabla_{\boldsymbol{X}} F_3 = \frac{p^2}{\Gamma v_A}\frac{(-\cos\phi')}{(b^2+v_A^2t^2)^{5/2}}\left[\frac{b^4-10b^2v_A^2t^2+4v_A^4t^4}{b(b^2+v_A^2t^2)} + \frac{-b^6+11b^4v_A^2t^2+4b^2v_A^4t^4-8v_A^6t^6}{(b^2+v_A^2t^2)^{5/2}}\right]. \tag{S78}$$

Applying the inverse rotation matrix to $\boldsymbol{X}^{(1)}\cdot\nabla_{\boldsymbol{X}}\boldsymbol{F}$ we obtain the FSF for the general scattering event in Fig. 1b

$$\boldsymbol{f}_{\boldsymbol{b}}^{O(2)}(t)=\begin{pmatrix}\sin\theta\cos\phi[\boldsymbol{X}^{(1)}\cdot\nabla_{\boldsymbol{X}}]F_1-\sin\phi[\boldsymbol{X}^{(1)}\cdot\nabla_{\boldsymbol{X}}]F_2-\cos\theta\cos\phi[\boldsymbol{X}^{(1)}\cdot\nabla_{\boldsymbol{X}}]F_3\\ \sin\theta\sin\phi[\boldsymbol{X}^{(1)}\cdot\nabla_{\boldsymbol{X}}]F_1+\cos\phi[\boldsymbol{X}^{(1)}\cdot\nabla_{\boldsymbol{X}}]F_2-\cos\theta\sin\phi[\boldsymbol{X}^{(1)}\cdot\nabla_{\boldsymbol{X}}]F_3\\ \cos\theta[\boldsymbol{X}^{(1)}\cdot\nabla_{\boldsymbol{X}}]F_1+\sin\theta[\boldsymbol{X}^{(1)}\cdot\nabla_{\boldsymbol{X}}]F_3\end{pmatrix}. \tag{S79}$$

We write explicitly only its projection along the direction $\boldsymbol{e}_x$. Using Eqs. (S76–S78) and (S79) we obtain

$$\begin{aligned}f_{\boldsymbol{b}}^{O(2)}(t)=\frac{p^2}{\Gamma v_{\mathrm{A}}}\frac{1}{(b^2+v_{\mathrm{A}}^2t^2)^{5/2}}\Bigg\{&\left[\frac{3v_{\mathrm{A}}t(2v_{\mathrm{A}}^2t^2-3b^2)}{b^2+v_{\mathrm{A}}^2t^2}+\frac{bv_{\mathrm{A}}t(11b^2-10v_{\mathrm{A}}^2t^2)}{(b^2+v_{\mathrm{A}}^2t^2)^{3/2}}\right]\mathcal{A}(\theta,\phi,\phi')\\&+\left[\frac{b^4-10b^2v_{\mathrm{A}}^2t^2+4v_{\mathrm{A}}^4t^4}{b(b^2+v_{\mathrm{A}}^2t^2)}+\frac{-b^6+11b^4v_{\mathrm{A}}^2t^2+4b^2v_{\mathrm{A}}^4t^4-8v_{\mathrm{A}}^6t^6}{(b^2+v_{\mathrm{A}}^2t^2)^{5/2}}\right]\mathcal{B}(\theta,\phi,\phi')\Bigg\}.\end{aligned} \tag{S80}$$

with the auxiliary functions $\mathcal{A},\mathcal{B}$ defined in Eqs (S36, S37). Its time integral is given by

$$\int_{-\infty}^{\infty}\mathrm{d}t\,f_{\boldsymbol{b}}^{O(2)}(t)=-\frac{\pi}{16}\frac{p^2}{b^3\Gamma v_{\mathrm{A}}^2}\mathcal{B}(\theta,\phi,\phi'). \tag{S81}$$

Thus, the tracer total displacement during the scattering event is generally non null at second order approximation, because its trajectory is not a closed loop. Only for injection angles $\{\theta,\phi,\phi'\}$ satisfying the condition $\mathcal{B}(\theta,\phi,\phi')=0$, $f_{\boldsymbol{b}}^{O}$ is symmetric and its time integral, as well as the total displacement of the tracer in the direction $\boldsymbol{e}_x$, is null. Combining Eqs. (S70, S80) yields the force shape function up to second perturbation order

$$\begin{aligned}f_{\boldsymbol{b}}^{O}(t)=\frac{p}{(b^2+v_{\mathrm{A}}^2t^2)^{5/2}}\Bigg\{&\left[b(2v_{\mathrm{A}}^2t^2-b^2)+\frac{p}{\Gamma v_{\mathrm{A}}}\left(\frac{3v_{\mathrm{A}}t(2v_{\mathrm{A}}^2t^2-3b^2)}{b^2+v_{\mathrm{A}}^2t^2}+\frac{bv_{\mathrm{A}}t(11b^2-10v_{\mathrm{A}}^2t^2)}{(b^2+v_{\mathrm{A}}^2t^2)^{3/2}}\right)\right]\mathcal{A}(\theta,\phi,\phi')\\&+\left[v_{\mathrm{A}}t(2v_{\mathrm{A}}^2t^2-b^2)+\frac{p}{\Gamma v_{\mathrm{A}}}\left(\frac{b^4-10b^2v_{\mathrm{A}}^2t^2+4v_{\mathrm{A}}^4t^4}{b(b^2+v_{\mathrm{A}}^2t^2)}+\frac{-b^6+11b^4v_{\mathrm{A}}^2t^2+4b^2v_{\mathrm{A}}^4t^4-8v_{\mathrm{A}}^6t^6}{(b^2+v_{\mathrm{A}}^2t^2)^{5/2}}\right)\right]\mathcal{B}(\theta,\phi,\phi')\Bigg\}.\end{aligned} \tag{S82}$$

Introducing the dimensionless variables (S27), Eq. (S82) yields Eqs. (S33-S35).

B. Characteristic functional of the coloured Poisson noise

We assume to observe N random scattering events at times $\{\tau_j\}$ specified by the set of parameters $\{\boldsymbol{b}_j\}$ with $j=1,\dots,N$ in the time interval $[-T,T]$. Each $\boldsymbol{b}_j$ contains an impact parameter $b_j\in(0,\infty)$ and a sequence of injection angles that specifies the geometry of the scattering. For instance, in 3D these are $\{\theta_j,\phi_j,\phi_j'\}$ ($\theta_j\in[0,\pi]$ and $\phi_j,\phi_j'\in[0,2\pi]$) (see Fig. S4b). If no other events occur, the total force at time $t>T$ projected along the direction $\boldsymbol{e}_x$ is

$$\boldsymbol{e}_x\cdot\boldsymbol{F}(t)=\sum_{j=1}^{N}f_{\boldsymbol{b}_j}(t-\tau_j). \tag{S83}$$

Its characteristic function is then given by (g is a generic test function) [43]

$$\chi_{\mathrm{d}}[g(s)]=\exp\left(i\sum_{j=1}^{N}\int_{-T}^{T}g(s)f_{\boldsymbol{b}_j}(s-\tau_j)\,\mathrm{d}s\right). \tag{S84}$$

However, the quantities $\{\tau_j,\boldsymbol{b}_j\}$ are in general random. We assume different parameter sets $\{\boldsymbol{b}_j\}$ to be independent between themselves and of τ_j, but we allow each of their components to be dependent for fixed j. We then call $\lambda(\boldsymbol{b})\,\mathrm{d}\boldsymbol{b}$ with the volume element $\mathrm{d}\boldsymbol{b}\equiv|J_{\boldsymbol{b}}|\,\mathrm{d}b\,\mathrm{d}\theta\,\mathrm{d}\phi\,\mathrm{d}\phi'$ the probability of sampling one such parameter set and assume that $\{\tau_j\}$ are independent and uniformly distributed in $[-T,T]$. Upon averaging over their realizations, the characteristic function of the projected force (S83) becomes

$$\overline{\chi}[g(s)]=\prod_{j=1}^{N}\frac{1}{2T}\int_{-T}^{T}\mathrm{d}\tau_j\int\mathrm{d}\boldsymbol{b}_j\lambda(\boldsymbol{b}_j)\exp\left(i\int_{-T}^{T}g(s)f_{\boldsymbol{b}_j}(s-\tau_j)\,\mathrm{d}s\right)$$

$$= \left[\frac{1}{2T}\int_{-T}^{T} \mathrm{d}\tau \int \mathrm{d}\boldsymbol{b}\lambda(\boldsymbol{b}) \exp\left(i\int_{-T}^{T} g(s) f_{\boldsymbol{b}}(s-\tau)\,\mathrm{d}s\right)\right]^{N}. \tag{S85}$$

Note that the second equality holds because of the independence of the random variables $\{\tau_j, \boldsymbol{b}_j\}$. Finally, the total number of events N occurring is also random. In details, we assume N to be Poisson distributed with constant mean rate c. This assumption is justified by the following properties [43]: (i) the occurrence of a scattering event is independent of the occurrence of any other event; and (ii) all the scattering events happen at a constant rate per unit time. These assumptions are most natural in the dilute and isotropic experimental conditions where the theory holds. Thus, the characteristic function is weighted by the probability of having N events, i.e., $\chi[g(s)] = \overline{\chi}[g(s)]e^{-2cT}[2cT]^N/N!$. If we average over all the possible number of events, i.e., by summing N to infinity, we obtain the series expansion of an exponential. Consequently, the characteristic functional of $\boldsymbol{e}_x \cdot \boldsymbol{F}(t)$ is

$$\log\chi[g(s)] = c\int_{-T}^{T} \mathrm{d}\tau \int \mathrm{d}\boldsymbol{b}\lambda(\boldsymbol{b})\left(-1 + e^{i\int_{-T}^{T} g(s) f_{\boldsymbol{b}}(s-\tau)\,\mathrm{d}s}\right). \tag{S86}$$

The previous equation describes the statistics of $\boldsymbol{e}_x \cdot \boldsymbol{F}$ if the force shape function $f_{\boldsymbol{b}}$ is short-range. In our model, instead, it is long-range (see Section VI A), such that $\boldsymbol{e}_x \cdot \boldsymbol{F}$ naturally depends also on future (and past) events happened for $t > T$ ($t < -T$). These are properly accounted for by taking the limit $T \to \infty$. In this limit we can no longer think in terms of a finite Poisson rate, because the number of events diverges as $2cT \to \infty$. Nevertheless, the quantity $c\,\mathrm{d}t$ still specifies the probability that a scattering event occurs in an infinitesimal time interval. Assuming that distinct scattering events do not overlap, we can fix $c = 1$. Therefore, we obtain

$$\log\chi[g(s)] = \int_{-\infty}^{\infty} \mathrm{d}\tau \int \mathrm{d}\boldsymbol{b}\lambda(\boldsymbol{b})\left(-1 + e^{i\int_{-\infty}^{\infty} g(s) f_{\boldsymbol{b}}(s-\tau)\,\mathrm{d}s}\right). \tag{S87}$$

The function $\lambda(\boldsymbol{b})$ depends on the specific problem at hand and was derived in Section II A for our case.

C. Consistency with the Holtsmark-type theory for short timescales

The theoretical argument underlying the Holtsmark theory is the following: Consider a physical body that is surrounded by m other bodies, each generating a static force field $\boldsymbol{F}_i$. Thus, the reference body is displaced by the superposition of the singular static force fields $\boldsymbol{F} \equiv \sum_i \boldsymbol{F}_i$. This theory was originally proposed to model the motion of gravitational bodies [44], but recently it was also adapted to model passive tracers in active suspensions [10, 24]. Below we outline this theory in the context of active suspensions and in particular we derive the tail scaling behaviour of the tracer displacement statistics.

We assume that the tracer particle is located at $\boldsymbol{X}_0 = (0,0,0)$ at the initial time $t = 0$ and that m particles are randomly distributed around it in the volume L^3. Their direction of motion is specified by $\boldsymbol{v}_i$ satisfying $|\boldsymbol{v}_i| = v_A$. The distribution of each active particle is assumed to be spatially uniform for $\boldsymbol{x}_i$ and spherically uniform for $\boldsymbol{v}_i$:

$$P(\boldsymbol{x}_i, \boldsymbol{v}_i) = \frac{1}{4\pi v_A^2 L^3}\delta(|\boldsymbol{v}_i| - v_A). \tag{S88}$$

Here we introduce a spherical coordinate system for $\boldsymbol{x}_i$ as

$$\boldsymbol{x}_i \equiv b_i \begin{pmatrix} \sin\theta_i\cos\phi_i \\ \sin\theta_i\sin\phi_i \\ \cos\theta_i \end{pmatrix}. \tag{S89}$$

We also introduce a set of orthogonal vectors as

$$\boldsymbol{e}_{b_i} \equiv \frac{\partial x_i}{\partial b_i} = \begin{pmatrix} \sin\theta_i\cos\phi_i \\ \sin\theta_i\sin\phi_i \\ \cos\theta_i \end{pmatrix}, \quad \boldsymbol{e}_{\theta_i} \equiv \frac{1}{b_i}\frac{\partial x_i}{\partial \theta_i} = \begin{pmatrix} \cos\theta_i\cos\phi_i \\ \cos\theta_i\sin\phi_i \\ -\sin\theta_i \end{pmatrix}, \quad \boldsymbol{e}_{\phi_i} \equiv \frac{1}{b_i\sin\theta_i}\frac{\partial x_i}{\partial \phi_i} = \begin{pmatrix} -\sin\phi_i \\ \cos\phi_i \\ 0 \end{pmatrix}. \tag{S90}$$

The velocity vector $\boldsymbol{v}_i$ is decomposed into the following form:

$$\boldsymbol{v}_i = v_i\sin\theta_i'\cos\phi_i'\boldsymbol{e}_{\theta_i'} + v_i\sin\theta_i'\sin\phi_i'\boldsymbol{e}_{\phi_i'} + v_i\cos\theta_i'\boldsymbol{e}_{b_i}, \tag{S91}$$

which corresponds to a spherical-coordinate representation by $(v_i, \theta_i', \phi_i')$. The force exerted by the active particles is then represented by

$$\boldsymbol{F} = \sum_{i=1}^{m} \frac{p}{b_i^2}\left[3\frac{(\boldsymbol{v}_i\cdot\boldsymbol{x}_i)^2}{v_i^2 b_i^2} - 1\right]\frac{\boldsymbol{x}_i}{b_i} = \sum_{i=1}^{m}\frac{p}{b_i^2}\left[3\cos^2\theta_i' - 1\right]\frac{\boldsymbol{x}_i}{b_i} \tag{S92}$$

with $b_i \equiv |\boldsymbol{x}_i - \boldsymbol{X}_0| = |\boldsymbol{x}_i|$. Because the random variables $\{(\boldsymbol{x}_i, \boldsymbol{v}_i)\}$ are independent, the characteristic function of the x-component of $\boldsymbol{F}$ is given by

$$\widehat{p}(k) = \langle e^{ik\boldsymbol{F}\cdot\boldsymbol{e}_x}\rangle = \langle e^{ik\sum_{i=1}^m p[3\cos^2\theta_i'-1](\boldsymbol{x}_i\cdot\boldsymbol{e}_x)/b_i^3}\rangle = \left(\langle e^{ikp[3\cos^2\theta_i'-1](\boldsymbol{x}_i\cdot\boldsymbol{e}_x)/b_i^3}\rangle\right)^m. \tag{S93}$$

By taking the thermodynamic limit $L\to\infty$ with the density kept constant ($\rho = m/L^3$ =const.) and by writing out the ensemble averages with the Jacobian relations $d\boldsymbol{x}_i = b^2\sin\theta_i\,\mathrm{d}b\,\mathrm{d}\theta_i\,\mathrm{d}\phi_i$ and $d\boldsymbol{v}_i = v_A^2\sin\theta_i'\,\mathrm{d}b\,\mathrm{d}\theta_i'\,\mathrm{d}\phi_i'$, we obtain

$$\begin{aligned}\widehat{p}(k) &= \left\{1 + \frac{1}{m}\left[m(\langle e^{ikp[3\cos^2\theta_i'-1](\boldsymbol{x}_i\cdot\boldsymbol{e}_x)/b_i^3}\rangle - 1)\right]\right\}^m \approx \exp\left[m\left(\langle e^{ikp[3\cos^2\theta_i'-1](\boldsymbol{x}_i\cdot\boldsymbol{e}_x)/b_i^3}\rangle - 1\right)\right]\\ &\approx \exp\left[\frac{\rho}{4\pi}\int_0^\infty b^2\,\mathrm{d}b\int_0^\pi \sin\theta\,\mathrm{d}\theta\int_0^{2\pi}\mathrm{d}\phi\int_0^\pi\sin\theta'\,\mathrm{d}\theta'\int_0^{2\pi}\mathrm{d}\phi'\left(\exp\left[\frac{ikp}{b^2}\{3\cos^2\theta'-1\}\sin\theta\cos\phi\right] - 1\right)\right].\end{aligned} \tag{S94}$$

Here we use identities,

$$\int_0^{2\pi}[e^{ik\cos\phi} - 1]\,\mathrm{d}\phi = 2\pi[J_0(|k|) - 1], \quad \int_0^\pi [J_0(|k\sin\theta|) - 1]\sin\theta\,\mathrm{d}\theta = 2\left(\frac{\sin|k|}{|k|} - 1\right) \tag{S95}$$

with J_0 the Bessel function of first kind. We then obtain

$$\begin{aligned}\log\widehat{p}(k) &\approx \pi\rho\int_0^\infty b^2\,\mathrm{d}b\int_0^\pi\sin\theta\,\mathrm{d}\theta\int_0^\pi\sin\theta'\,\mathrm{d}\theta'\left[J_0\left(\frac{|pk\{3\cos^2\theta'-1\}\sin\theta|}{b^2}\right) - 1\right]\\ &\approx 2\pi\rho\int_0^\infty b^2\,\mathrm{d}b\int_0^\pi\sin\theta'\,\mathrm{d}\theta'\left[\frac{b^2}{|pk|\{3\cos^2\theta'-1\}|}\sin\left(\frac{|pk|\{3\cos^2\theta'-1\}|}{b^2}\right) - 1\right]\\ &\approx 4\pi\rho|pk|^{3/2}\int_0^\infty x^2\,\mathrm{d}x\int_0^1\mathrm{d}y\left[\frac{x^2}{|\{3y^2-1\}|}\sin\frac{|\{3y^2-1\}|}{x^2} - 1\right]\\ &\approx -\widetilde{C}_H\rho|pk|^{3/2}\end{aligned} \tag{S96}$$

with $y\equiv\cos\theta'$, $x\equiv(|pk|)^{-1/2}b$, and the coefficient

$$\widetilde{C}_H \equiv -4\pi\int_0^\infty x^2\,\mathrm{d}x\int_0^1\mathrm{d}y\left[\frac{x^2}{|\{3y^2-1\}|}\sin\frac{|\{3y^2-1\}|}{x^2} - 1\right] \approx 3.21. \tag{S97}$$

Given that the displacement ΔX is related to the force F_x by $\Delta X/\Delta t = F_x/\Gamma$ for the overdamped regime for short time Δt, the cumulant function for the tracer displacement for x-direction is given by

$$\log\widehat{P}_{\Delta t}(k) \approx -\widetilde{C}_H\rho\left(\frac{|p|}{\Gamma}\right)^{3/2}\Delta t^{3/2}|k|^{3/2}. \tag{S98}$$

This result is consistent with Eq. (4) derived from our coloured Poisson model, not only for the scaling exponent but also for the coefficient (see Eqs. (S108, S109)).

The consistency between the Holtsmark-type static theory and our dynamical approach is not trivial: The Holtsmark theory in fact relies on a specific assumption, namely that all particles are uniformly and independently distributed at any time and that their dynamics can be effectively neglected. Our dynamical theory based on the coloured Poisson model can thus be regarded as the foundation of such a static approach.

D. Asymptotic behaviour of displacement statistics for short timescales

For short timescale $\Delta t \ll \tau_{\mathrm{H}}$ we can make the approximation $\int_0^{\Delta t} f_{\boldsymbol{b}}(s-t)\,\mathrm{d}s \approx \Delta t f_{\boldsymbol{b}}(-t)$ in the exponential of Eq. (S40), where the FSF is prescribed as in Eq. (S22). Expressing Eq. (S40) in the dimensionless coordinates (S27)

by using the exact rescaled expression of $f_{\boldsymbol{b}}^{O}$ given in Eq. (S33) and neglecting the thermal contribution, we obtain

$$\log \widehat{P}_{\Delta t}(k) = \frac{\rho b^{*3}}{4\pi} \int_{-\infty}^{\infty} \mathrm{d}y \int_{d/b^*}^{\infty} \mathrm{d}x\, x \int \mathrm{d}\boldsymbol{\Omega} \left[-1 + e^{i\widetilde{k}\Delta y f_{\boldsymbol{x}}^{\mathrm{O}}(y)} \right], \tag{S99}$$

where $\widetilde{k} = kb^*$, $\Delta y = \Delta t/\tau_{\mathrm{H}}$ and $\mathrm{d}\boldsymbol{\Omega} \equiv \sin\theta\, \mathrm{d}\theta\, \mathrm{d}\phi\, \mathrm{d}\phi'$. To get its asymptotic behaviour, we perform a second coordinate change $z = y/x$. Eqs. (S34, S35) then become

$$g_1(x,z) = \frac{p}{|p|}\frac{1}{x^2}\frac{(2z^2-1)}{(1+z^2)^{5/2}} + \frac{1}{x^4}\left[\frac{3z(2z^2-3)}{(1+z^2)^{7/2}} + \frac{z(11-10z^2)}{(1+z^2)^4}\right], \tag{S100}$$

$$g_2(x,z) = \frac{p}{|p|}\frac{1}{x^2}\frac{z(2z^2-1)}{(1+z^2)^{5/2}} + \frac{1}{x^4}\left[\frac{-1+11z^2+4z^4-8z^6}{(1+z^2)^5} + \frac{1-10z^2+4z^4}{(1+z^2)^{7/2}}\right]. \tag{S101}$$

Keeping only terms of order x^{-2}, we then obtain:

$$f_{\boldsymbol{x}}^{\mathrm{O}}(y) \approx \frac{p}{|p|}\frac{1}{x^2}\frac{(2z^2-1)}{(1+z^2)^{5/2}}[\mathcal{A}(\theta,\phi,\phi') + z\mathcal{B}(\theta,\phi,\phi')]. \tag{S102}$$

Using this approximation and the identity

$$\int_0^{2\pi} [e^{ik(a\cos\phi + b\sin\phi)} - 1]\, \mathrm{d}\phi = 2\pi[J_0(|k|\sqrt{a^2+b^2}) - 1], \tag{S103}$$

the displacement PDF simplifies to

$$\begin{aligned}\log \widehat{P}_{\Delta t}(k) &\approx \frac{\rho b^{*3}}{4\pi} \int_{-\infty}^{\infty} \mathrm{d}z \int_{d/b^*}^{\infty} \mathrm{d}x\, x^2 \int \mathrm{d}\boldsymbol{\Omega} \left\{ -1 + \exp\left[i\frac{p}{|p|}\frac{\widetilde{k}\Delta y}{x^2}\frac{(2z^2-1)}{(1+z^2)^{5/2}}(\mathcal{A}(\theta,\phi,\phi') + z\mathcal{B}(\theta,\phi,\phi')) \right] \right\} \\ &\approx \frac{\rho b^{*3}}{2} \int_{-\infty}^{\infty} \mathrm{d}z \int_{d/b^*}^{\infty} \mathrm{d}x\, x^2 \int_0^{\pi} \mathrm{d}\theta \sin\theta \int_0^{2\pi} \mathrm{d}\phi' \left[-1 + J_0\left(\frac{|\widetilde{k}|\Delta y}{x^2}\frac{|2z^2-1|}{(1+z^2)^{5/2}} h(z,\theta,\phi') \right) \right]\end{aligned} \tag{S104}$$

with the auxiliary function

$$h(z,\theta,\phi') \equiv \sqrt{(z\sin\phi')^2 + (\sin\theta + z\cos\theta\cos\phi')^2}. \tag{S105}$$

Neglecting the truncation, i.e., setting $d \approx 0$, and performing the change of variable $x' = x/\sqrt{|\widetilde{k}|\Delta y}$ yields

$$\log \widehat{P}_{\Delta t}(k) \approx \frac{\rho b^{*3}}{2}(|\widetilde{k}|\Delta y)^{3/2} \int_{-\infty}^{\infty} \mathrm{d}z \int_0^{\infty} \mathrm{d}x' x'^2 \int_0^{\pi} \mathrm{d}\theta \sin\theta \int_0^{2\pi} \mathrm{d}\phi' \left[-1 + J_0\left(\frac{1}{x'^2}\frac{|2z^2-1|}{(1+z^2)^{5/2}} h(z,\theta,\phi') \right) \right]. \tag{S106}$$

The remaining integral is now only a numerical factor. Therefore, we write

$$\log \widehat{P}_{\Delta t}(k) \approx -\widetilde{C}_{\mathrm{H}} \rho b^{*3} \Delta y^{3/2} |\widetilde{k}|^{3/2} \tag{S107}$$

where the coefficient $\widetilde{C}_{\mathrm{H}}$ is equal to

$$\widetilde{C}_{\mathrm{H}} \equiv \frac{1}{2} \int_{-\infty}^{\infty} \mathrm{d}z \int_0^{\infty} \mathrm{d}x' x'^2 \int_0^{\pi} \mathrm{d}\theta \sin\theta \int_0^{2\pi} \mathrm{d}\phi' \left[1 - J_0\left(\frac{1}{x'^2}\frac{|2z^2-1|}{(1+z^2)^{5/2}} h(z,\theta,\phi') \right) \right] \approx 3.21. \tag{S108}$$

Transforming back to dimensional coordinates yields the scaling equation (S41) (see Eq. (S143) for details on the asymptotic formula)

$$\log \widehat{P}_{\Delta t}(k) \approx -\widetilde{C}_{\mathrm{H}} \rho \left(\frac{|p|}{\Gamma} \right)^{3/2} \Delta t^{3/2} |k|^{3/2} \longrightarrow P_{\Delta t}(|\Delta X|) \approx 0.96 \rho \left(\frac{|p|}{\Gamma} \right)^{3/2} \Delta t^{3/2}\, |\Delta X|^{-5/2}. \tag{S109}$$

E. Asymptotic behaviour of displacement statistics in the Markovian regime

For the intermediate timescale $\tau_{\rm H} \ll \Delta t \ll \tau_{\rm C}$, the integral of the FSF can be approximated as

$$\int_0^{\Delta t} f_{\boldsymbol{b}}(s-t')\,\mathrm{d}s \approx y(\boldsymbol{b})\Theta(t')\Theta(\Delta t - t'), \tag{S110}$$

where $y(\boldsymbol{b}) \equiv \int_{-\infty}^{\infty} f_{\boldsymbol{b}}(s)\,\mathrm{d}s$ is the total displacement of the tracer after the scattering. Using Eqs. (S22, S81), we obtain

$$y(\boldsymbol{b}) \equiv \begin{cases} -\frac{\pi}{16}\frac{p^2}{\Gamma v_{\rm A}^2}\frac{\mathcal{B}(\theta,\phi,\phi')}{|b|^3} & |b| > d \\ 0 & |b| \le d \end{cases}. \tag{S111}$$

Applying it to Eq. (S40) (where for simplicity we neglect the thermal contribution) and writing the result in the dimensionless coordinates (S27) yields

$$\log \widehat{P}_{\Delta t}(k) \approx \frac{\rho {b^*}^3}{4\pi}\Delta y \int_{d/b^*}^{\infty} \mathrm{d}x\, x \int \mathrm{d}\boldsymbol{\Omega}\,[-1 + e^{i\tilde{k}y(\boldsymbol{x})}], \qquad y(\boldsymbol{x}) \equiv -\frac{\pi}{16}\frac{\mathcal{B}(\theta,\phi,\phi')}{x^3}, \tag{S112}$$

with $\tilde{k} = kb^*$, $\Delta y = \Delta t/\tau_{\rm H}$. Neglecting the truncation, we can study the power-law part of the distribution: Employing the identity (S103), we obtain

$$\begin{aligned} \log \widehat{P}_{\Delta t}(k) &\approx \frac{\rho {b^*}^3}{2}\Delta y \int_0^{\infty} \mathrm{d}x x \int_0^{\pi} \mathrm{d}\theta \sin\theta \int_0^{2\pi} \mathrm{d}\phi' \left[-1 + J_0\left(\frac{\pi}{16}\frac{|\tilde{k}|}{x^3}\sqrt{1-(\sin\theta\cos\phi')^2}\right)\right] \\ &\approx \frac{\rho {b^*}^3}{2}\left(\frac{\pi}{16}|\tilde{k}|\right)^{2/3}\Delta y \int_0^{\infty} \mathrm{d}x' x' \int_0^{\pi} \mathrm{d}\theta \sin\theta \int_0^{2\pi} \mathrm{d}\phi' \left[-1 + J_0\left({x'}^{-3}\sqrt{1-(\sin\theta\cos\phi')^2}\right)\right], \end{aligned} \tag{S113}$$

where in the second line we change variable as $x' = x/\left(\frac{\pi}{16}|\tilde{k}|\right)^{1/3}$. The remaining integral is just a numerical coefficient. Therefore, we can write

$$\log \widehat{P}_{\Delta t}(k) \approx -C_{\rm S}\rho {b^*}^3 \Delta y |\tilde{k}|^{2/3} \tag{S114}$$

with the numerical coefficient (we make the change of variables $s_1 = \cos\theta$, $s_2 = \cos\phi'$)

$$C_{\rm S} \equiv 4\left(\frac{\pi}{16}\right)^{2/3}\int_0^{\infty}\mathrm{d}x' x' \int_0^1 \mathrm{d}s_1 \int_0^1 \frac{\mathrm{d}s_2}{\sqrt{1-s_2^2}}\left[1 - J_0\left({x'}^{-3}\sqrt{1-s_2^2+s_1^2 s_2^2}\right)\right] \approx 0.85. \tag{S115}$$

Transforming back to dimensional coordinates yields Eq. (S41) (see Eq. (S143) for details on the asymptotic formula)

$$\log \widehat{P}_{\Delta t}(k) \approx -C_{\rm S}\rho v_{\rm A}\Delta t\left(\frac{|p|}{\Gamma v_{\rm A}}\right)^{4/3}|k|^{2/3} \longrightarrow P_{\Delta t}(|\Delta X|) \approx 0.21\rho v_{\rm A}\Delta t\left(\frac{|p|}{\Gamma v_{\rm A}}\right)^{4/3}|\Delta X|^{-5/3}. \tag{S116}$$

F. Asymptotic behaviour of displacement statistics in the Central Limit Theorem regime

For the timescale $\tau_{\rm C} \ll \Delta t$, the truncation in Eq. (S112) has to be considered. Expanding the Bessel function at first non null order in $\tilde{k}$, we obtain

$$\begin{aligned} \log \widehat{P}_{\Delta t}(k) &\approx -\frac{\rho {b^*}^3}{8}\left(\frac{\pi}{16}\right)^2|\tilde{k}|^2\Delta y \int_{d/b^*}^{\infty}\frac{\mathrm{d}x}{x^5}\int_0^{\pi}\mathrm{d}\theta\sin\theta\int_0^{2\pi}\mathrm{d}\phi'[1-(\sin\theta\cos\phi')^2] \\ &\approx -\frac{4}{3}\left(\frac{\pi}{16}\right)^3\rho {b^*}^3\left(\frac{b^*}{d}\right)^4\Delta y|\tilde{k}|^2. \end{aligned} \tag{S117}$$

We rewrite this result as

$$\log \widehat{P}_{\Delta t}(k) \approx -\frac{\Sigma^2}{2}\Delta y|\tilde{k}|^2, \qquad \Sigma^2 \equiv \frac{8}{3}\left(\frac{\pi}{16}\right)^3\rho {b^*}^3\left(\frac{b^*}{d}\right)^4. \tag{S118}$$

Transforming back to dimensional coordinates yields

$$\log \widehat{P}_{\Delta t}(k) \approx -\frac{\sigma_a^2}{2}\Delta t\,|k|^2 \longrightarrow P_{\Delta t}(|\Delta X|) \propto e^{-\Delta X^2/(2\sigma_a^2)}, \tag{S119}$$

with the positive parameter

$$\sigma_a^2 \equiv \frac{8}{3}\left(\frac{\pi}{16}\right)^3 \frac{\rho v_{\rm A}}{d^4}\left(\frac{|p|}{\Gamma v_{\rm A}}\right)^4. \tag{S120}$$

Including the contribution of the thermal noise finally yields Eq. (S41)

$$\log \widehat{P}_{\Delta t}(k) \approx -\sigma^2\Delta t|k|^2 \longrightarrow P_{\Delta t}(|\Delta X|) \propto e^{-\Delta X^2/(2\sigma^2)} \tag{S121}$$

with $\sigma^2 \equiv 2D_0 + \sigma_a^2$.

G. Asymptotic scaling behaviour of the mean square displacement

For convenience, we consider only the athermal term in the rhs of Eq. (S43). In dimensionless coordinates this is written as

$$\mathrm{MSD}(\Delta y) = \frac{\rho b^{*5}}{4\pi}\int_{-\infty}^{\infty}\mathrm{d}y\int_{d/b^*}^{\infty}\mathrm{d}x\,x\int \mathrm{d}\boldsymbol{\Omega}\left[\int_0^{\Delta y}\mathrm{d}y' f_{\boldsymbol{x}}^{O}(y'-y)\right]^2, \tag{S122}$$

where the FSF is specified by Eqs. (S33-S35), $\boldsymbol{x} \equiv (x,\theta,\phi,\phi')$ and $\mathrm{d}\boldsymbol{\Omega} \equiv \sin\theta\,\mathrm{d}\theta\,\mathrm{d}\phi\,\mathrm{d}\phi'$. Using these definitions and integrating out the angular variables, we obtain ($\int \mathrm{d}\boldsymbol{\Omega}\,[\mathcal{A}(\theta,\phi,\phi')]^2 = \int \mathrm{d}\boldsymbol{\Omega}\,[\mathcal{B}(\theta,\phi,\phi')]^2 = 8\pi^2/3$, $\int \mathrm{d}\boldsymbol{\Omega}\,[\mathcal{A}(\theta,\phi,\phi')\mathcal{B}(\theta,\phi,\phi')] = 0$)

$$\mathrm{MSD}(\Delta y) = \frac{2\pi}{3}\rho b^{*5}\int_{-\infty}^{\infty}\mathrm{d}y\int_{d/b^*}^{\infty}\mathrm{d}x\,x\sum_{i=1}^{2}\left[\int_0^{\Delta y}\mathrm{d}y' g_i(x,y'-y)\right]^2. \tag{S123}$$

Adopting coordinate $z' = (y'-y)/x$, the equation is further simplified as

$$\mathrm{MSD}(\Delta y) = \frac{2\pi}{3}\rho b^{*5}\int_{-\infty}^{\infty}\mathrm{d}y\int_{d/b^*}^{\infty}\mathrm{d}x\,x\sum_{i=1}^{2}\left[\int_{-y/x}^{(\Delta y-y)/x}\mathrm{d}z'\tilde{g}_i(x,z')\right]^2, \tag{S124}$$

where the auxiliary functions are defined as $\tilde{g}_i(x,z) = x g_i(x,z)$, and $g_i(x,z)$ are given in Eqs. (S100, S101).

The coefficient for small Δy is then obtained as follows: For $\Delta y \ll 1$, we have

$$\int_{-y/x}^{(\Delta y-y)/x}\mathrm{d}z'\tilde{g}_i(x,z') \approx \frac{\Delta y}{x}\tilde{g}_i\Big(x,-\frac{y}{x}\Big), \tag{S125}$$

such that the MSD becomes

$$\mathrm{MSD}(\Delta y) \approx \frac{2\pi}{3}\rho b^{*5}\Delta y^2\int_{-\infty}^{\infty}\mathrm{d}y\int_{d/b^*}^{\infty}\frac{\mathrm{d}x}{x}\sum_{i=1}^{2}\Big[\tilde{g}_i\Big(x,-\frac{y}{x}\Big)\Big]^2. \tag{S126}$$

Switching the order of integration and changing coordinates as $z = y/x$, we can rewrite it as

$$\mathrm{MSD}(\Delta y) \approx \frac{2\pi}{3}\rho b^{*5}\Delta y^2\int_{d/b^*}^{\infty}\mathrm{d}x\int_{-\infty}^{\infty}\mathrm{d}z\sum_{i=1}^{2}\left[\tilde{g}_i(x,-z)\right]^2. \tag{S127}$$

The remaining integrals can be performed exactly. In fact, we obtain

$$\mathrm{MSD}(\Delta y) \approx D_{\rm H}^{(2)}\rho b^{*5}\Delta y^2, \qquad D_{\rm H}^{(2)} \equiv \frac{5\pi^2}{24}\left(\frac{b^*}{d}\right) + \left(-\frac{6656\pi}{5775} + \frac{2879\pi^2}{7680}\right)\left(\frac{b^*}{d}\right)^5. \tag{S128}$$

In dimensional coordinates, Eq. (S128) yields the scaling behaviour predicted by Eq. (S44) in the Holtsmark regime.

For large Δy instead we apply the approximation Eq. (S110) to Eq. (S122). Therefore, we obtain

$$\begin{aligned}\mathrm{MSD}(\Delta y) &\approx \frac{\rho b^{*5}}{4\pi}\Delta y \int_{d/b^*}^{\infty} \mathrm{d}x\, x \int \mathrm{d}\boldsymbol{\Omega}[y(\boldsymbol{x})]^2 \\ &\approx \frac{\rho b^{*5}}{4\pi}\left(\frac{\pi}{16}\right)^2 \Delta y \int_{d/b^*}^{\infty} \frac{\mathrm{d}x}{|x|^5} \int \mathrm{d}\boldsymbol{\Omega}[\mathcal{B}(\theta,\phi,\phi')]^2, \end{aligned} \tag{S129}$$

where we used the definition of the function y in Eq. (S112). Solving the remaining integrals analytically, we obtain

$$\mathrm{MSD}(\Delta y) \approx D_{\mathrm{S}}^{(2)} \rho b^{*5} \Delta y, \qquad D_{\mathrm{S}}^{(2)} \equiv \frac{8}{3}\left(\frac{\pi}{16}\right)^3 \left(\frac{b^*}{d}\right)^4. \tag{S130}$$

In dimensional coordinates, Eq. (S130) yields the scaling behaviour predicted by Eq. (S44) in the scattering regime.

H. Asymptotic scaling behaviour of the non-Gaussian parameter

Because the asymptotic formulas for the second cumulant have already been computed in the previous section, it remains to calculate those for the fourth cumulant. In dimensionless coordinates, this is given by

$$\langle \Delta X^4 \rangle_{\mathrm{c}} = \frac{\rho b^{*7}}{4\pi} \int_{-\infty}^{\infty} \mathrm{d}y \int_{d/b^*}^{\infty} \mathrm{d}x\, x \int \mathrm{d}\boldsymbol{\Omega} \left[\int_0^{\Delta y} \mathrm{d}y' f_{\boldsymbol{x}}^{O}(y'-y)\right]^4, \tag{S131}$$

where the FSF is specified by Eqs. (S33-S35), $\boldsymbol{x} \equiv (x,\theta,\phi,\phi')$ and $\mathrm{d}\boldsymbol{\Omega} \equiv \sin\theta\,\mathrm{d}\theta\,\mathrm{d}\phi\,\mathrm{d}\phi'$. Using these definitions and integrating out the angular variables, we obtain (note that $\int \mathrm{d}\boldsymbol{\Omega}\,[\mathcal{A}(\theta,\phi,\phi')]^4 = \int \mathrm{d}\boldsymbol{\Omega}\,[\mathcal{B}(\theta,\phi,\phi')]^4 = 8\pi^2/5$, $\int \mathrm{d}\boldsymbol{\Omega}\,[\mathcal{A}(\theta,\phi,\phi')]^3\mathcal{B}(\theta,\phi,\phi') = \int \mathrm{d}\boldsymbol{\Omega}\,\mathcal{A}(\theta,\phi,\phi')[\mathcal{B}(\theta,\phi,\phi')]^3 = 0$ and $\int \mathrm{d}\boldsymbol{\Omega}\,[\mathcal{A}(\theta,\phi,\phi')]^2[\mathcal{B}(\theta,\phi,\phi')]^2 = 8\pi^2/15$)

$$\langle \Delta X^4 \rangle_{\mathrm{c}} = \frac{4\pi}{5}\rho b^{*7} \int_{-\infty}^{\infty} \mathrm{d}y \int_{d/b^*}^{\infty} \mathrm{d}x\, x \left\{\frac{1}{2}\sum_{i=1}^{2}\left[\int_0^{\Delta y} \mathrm{d}y' g_i(x,y'-y)\right]^4 + \prod_{i=1}^{2}\left[\int_0^{\Delta y} \mathrm{d}y' g_i(x,y'-y)\right]^2\right\}. \tag{S132}$$

Adopting coordinate $z' = (y'-y)/x$, the equation is further simplified as

$$\langle \Delta X^4 \rangle_{\mathrm{c}} = \frac{4\pi}{5}\rho b^{*7} \int_{-\infty}^{\infty} \mathrm{d}y \int_{d/b^*}^{\infty} \mathrm{d}x\, x \left\{\frac{1}{2}\sum_{i=1}^{2}\left[\int_{-y/x}^{(\Delta y-y)/x} \mathrm{d}z' \tilde{g}_i(x,z')\right]^4 + \prod_{i=1}^{2}\left[\int_{-y/x}^{(\Delta y-y)/x} \mathrm{d}z' \tilde{g}_i(x,z')\right]^2\right\}, \tag{S133}$$

with auxiliary functions again defined as $\tilde{g}_i(x,z) = x g_i(x,z)$, where $g_i(x,z)$ are given in Eqs. (S100, S101).

For $\Delta y \ll 1$, this equation can be solved analytically by employing the approximation (S125). In detail, we obtain

$$\langle \Delta X^4 \rangle_{\mathrm{c}} \approx \frac{4\pi}{5}\rho b^{*7} \Delta y^4 \int_{-\infty}^{\infty} \mathrm{d}y \int_{d/b^*}^{\infty} \frac{\mathrm{d}x}{x^3} \left\{\frac{1}{2}\sum_{i=1}^{2}\left[\tilde{g}_i\Big(x,-\frac{y}{x}\Big)\right]^4 + \prod_{i=1}^{2}\left[\tilde{g}_i\Big(x,-\frac{y}{x}\Big)\right]^2\right\}. \tag{S134}$$

Switching the order of integration and changing coordinates as $z = y/x$, we can rewrite it as

$$\langle \Delta X^4 \rangle_{\mathrm{c}} \approx \frac{4\pi}{5}\rho b^{*7} \Delta y^4 \int_{d/b^*}^{\infty} \frac{\mathrm{d}x}{x^2} \int_{-\infty}^{\infty} \mathrm{d}z \left\{\frac{1}{2}\sum_{i=1}^{2}[\tilde{g}_i(x,-z)]^4 + \prod_{i=1}^{2}[\tilde{g}_i(x,-z)]^2\right\}. \tag{S135}$$

The remaining integral in the rhs can be solved analytically in x and numerically in z. Thus, we write

$$\langle \Delta X^4 \rangle_{\mathrm{c}} \approx 3 D_{\mathrm{H}}^{(4)} \rho b^{*7} \Delta y^4, \qquad D_{\mathrm{H}}^{(4)} \approx \frac{4\pi}{15}\left[0.0462\left(\frac{b^*}{d}\right)^5 + 0.0124\left(\frac{b^*}{d}\right)^9 + 0.0005\left(\frac{b^*}{d}\right)^{13}\right]. \tag{S136}$$

Combining Eqs. (S128, S136), we finally obtain

$$\mathrm{NGP}(\Delta y) \approx \frac{1}{\rho b^{*3}} \frac{D_{\mathrm{H}}^{(4)}}{[D_{\mathrm{H}}^{(2)}]^2}. \tag{S137}$$

In dimensional coordinates, Eq. (S137) yields the scaling behaviour predicted by Eq. (S47) in the Holtsmark regime.

Conversely, for $\Delta y \gg 1$ we apply the approximation presented in Eq. (S110). In detail,

$$\begin{aligned}\langle \Delta X^4 \rangle_{\rm c} &\approx \frac{\rho b^{*7}}{4\pi} \Delta y \int_{d/b^*}^{\infty} {\rm d}x\, x \int {\rm d}\mathbf{\Omega}\, [y(\boldsymbol{x})]^4\,, \\ &\approx \frac{\rho b^{*7}}{4\pi} \left(\frac{\pi}{16}\right)^4 \Delta y \int_{d/b^*}^{\infty} \frac{{\rm d}x}{|x|^{11}} \int {\rm d}\mathbf{\Omega} [\mathcal{B}(\theta,\phi,\phi')]^4, \end{aligned} \tag{S138}$$

where we used the definition of y in dimensionless coordinates given in Eq. (S112). Solving the integrals yields

$$\langle \Delta X^4 \rangle_{\rm c} \approx 3 D_{\rm S}^{(4)} \rho b^{*7} \Delta y, \qquad D_{\rm S}^{(4)} \equiv \frac{16}{75} \left(\frac{\pi}{16}\right)^5 \left(\frac{b^*}{d}\right)^{10}. \tag{S139}$$

Finally, employing both Eqs. (S130, S139), we find

$$\mathrm{NGP}(\Delta y) \approx \frac{1}{\rho b^{*3} \Delta y} \frac{D_{\rm S}^{(4)}}{[D_{\rm S}^{(2)}]^2}. \tag{S140}$$

In dimensional coordinates, Eq. (S140) yields the scaling behaviour predicted by Eq. (S47) in the scattering regime.

I. Asymptotic tail behaviour of the Lévy distributions (S109, S116)

The characteristic functions of the probability densities (S109, S116) have the asymptotic form $\widehat{P}_{\Delta t}(k) \propto e^{-c|k|^\alpha}$ with $0 < \alpha \leq 2$, $c > 0$ that corresponds to a symmetric Lévy distribution [41]. Exact analytical expression for this density only exists for a few specific values of α. To derive the asymptotic scaling of the distribution tails, we use the symmetry properties of the characteristic function and write the Fourier inverse transform as

$$\begin{aligned} P_{\Delta t}(\Delta X) &= \frac{1}{\pi} \int_0^{\infty} {\rm d}k \cos(k|\Delta X|) e^{-ck^\alpha} \\ &= \frac{\alpha c}{\pi |\Delta X|} \int_0^{\infty} {\rm d}k \sin(k|\Delta X|) k^{\alpha-1} e^{-ck^\alpha} \\ &= \frac{c}{\pi |\Delta X|^{1+\alpha}} \int_0^{\infty} {\rm d}y \sin(y^{1/\alpha}) e^{-cy/|\Delta X|^\alpha}, \end{aligned} \tag{S141}$$

where we integrated by parts in the second line and performed the change of variables $y = (k|\Delta X|)^\alpha$ in the third one. The remaining integral in its rhs can be solved formally, such that we obtain the power series expansion [45]

$$P_{\Delta t}(\Delta X) = \frac{\alpha c}{\pi |\Delta X|^{1+\alpha}} \sum_{n=0}^{\infty} \frac{(-1)^n}{n!} \left(\frac{c}{|\Delta X|^\alpha}\right)^n \Pi(\alpha - 1 + \alpha n) \sin\left(\frac{\pi}{2}(1+n)\alpha\right) \tag{S142}$$

with $\Pi(\alpha) \equiv \int_0^\infty t^{\alpha-1} e^{-t}\, {\rm d}t$. For $|\Delta X| \gg 1$ the leading term is that with $n = 0$, i.e.,

$$P_{\Delta t}(\Delta X) \approx \frac{c\Pi(\alpha)}{\pi |\Delta X|^{1+\alpha}} \sin\left(\frac{\pi}{2}\alpha\right). \tag{S143}$$

[36] Press, W. H., Teukolsky, S. A., Vetterling, W. T. & Flannery, B. P. *The art of scientific computing* (1992).
[37] Résibois, P. & De Leener, M. Classical kinetic theory of fluids (1977).
[38] Shlesinger, M. F., Zaslavsky, G. M. & Frisch, U. Lévy flights and related topics in physics. *Lecture notes in physics* **450**, 52 (1995).
[39] Caceres, M. O. & Budini, A. A. The generalized Ornstein-Uhlenbeck process. *J. Phys. A* **30**, 8427 (1997).
[40] Hughes, B. D., Shlesinger, M. F. & Montroll, E. W. Random walks with self-similar clusters. *Proc. Natl. Acad. Sci.* **78**, 3287–3291 (1981).
[41] Applebaum, D. *Lévy processes and stochastic calculus* (Cambridge university press, 2009).
[42] Gardiner, C. Stochastic methods. *Springer Series in Synergetics (Springer-Verlag, Berlin, 2009)* (1985).
[43] Feynman, R. P., Hibbs, A. R. & Styer, D. *Quantum mechanics and path integrals* (Dover Publications, 2010).
[44] Chandrasekhar, S. Stochastic problems in physics and astronomy. *Rev. Mod. Phys.* **15**, 1 (1943).
[45] Wintner, A. The singularities of Cauchy's distributions. *Duke Mathematical Journal* **8**, 678–681 (1941).